HIGH-Q DIRECTIONAL-EMISSION WHISPERING-GALLERY-MODE MICROLASER SENSORS FOR LABEL-FREE BIODETECTION

ZHIZHENG WANG

MPhil

The Hong Kong Polytechnic University

2024

The Hong Kong Polytechnic University

Department of Electrical and Electronic Engineering

High-*Q* Directional-Emission Whispering-Gallery-Mode Microlaser Sensors for Label-Free Biodetection

Zhizheng WANG

A thesis submitted in partial fulfilment of the requirements for the degree of Master of Philosophy

March 2024

CERTIFICATE OF ORIGINALITY

I hereby declare that this thesis is my own work and that, to the best of my knowledge and belief, it reproduces no material previously published or written, nor material that has been accepted for the award of any other degree or diploma, except where due acknowledgement has been made in the text.

_____ (Signed)

Zhizheng WANG (Name of student)

Abstract

Optical microcavity is a kind of optical elements that has been widely proposed for high-sensitivity sensing in recent years. With the development of micro/nano fabrication technology and numerical simulation tools, many new sensing mechanisms of high quality-factor (*Q*) whispering-gallery-mode (WGM) microcavities have been demonstrated for various applications. Conventional optical microcavity sensors use circular microcavities. However, they can usually only be coupled with tapered optical fibers. This scheme requires a very accurate relative position between the tapered fiber and the microcavity, which means that such biosensors are prone to be disturbed by external environmental interferences. To solve this challenge, we demonstrated the deformed microcavities to develop high-*Q* WGM microlaser sensors with directional emission and far-field coupling capabilities for label-free biodetection.

Two different kinds of deformed microcavities are designed for WGM microlaser sensing. The first is the Limacon-shaped microcavity, which has been proved to have a unidirectional emission around 0° direction. Another deformed microcavity we employed is elliptical microcavity. Due to the axial symmetry of its contour, it allows directional emission in four different directions. Numerical simulations using COMSOL have been systematically carried out to calculate the distribution of WGMs and their sensitivity to the refractive index change of external medium as well as their directional emission behaviors.

These WGM microlaser sensors with weakly deformed microcavities have been experimentally fabricated and demonstrated for label-free biodetection. An optical 3D microprinting technology using a digital micromirror device (DMD) as optical pattern generator and a UV lamp as a projection light source has been established to rapidly fabricate different designs of WGM microcavities. A negative photoresist SU-8 was used to fabricate the designed WGM microcavities and microlaser sensors. A dynamic exposure scheme is

developed to directly print 3D SU-8 microstructures for WGM microcavity and microlaser fabrication.

The fabricated WGM microlaser sensors have been tested by using an own-established pumping test setup. A 532-nm pulsed laser was employed to pump these 3D micro-printed WGM microlasers. The spectral peak bandwidths of the fabricated WGM microlasers' emission spectra were measured to be as narrow as about 20 pm, which corresponds to a very high Q value of around 2.51×10^4. In the experiments, WGM microlasers of both Limacon-shaped and elliptical microcavities showed directional emission clearly. The sensitivities of these WGM microlaser sensors were measured and compared with numerical simulation results.

The biodetection ability of such 3D micro-printed WGM microlaser sensors has been demonstrated in experiments. The fabricated WGM microlaser sensors were modified with antibodies to specifically detect human immunoglobulin G (IgG) in the solution. When the antigen-antibody binding reaction occurs on the surface of WGM microlaser sensors, the wavelength of the WGM of microlaser sensor was shifted, allowing for specific detection of human IgG. The experiments revealed that the fabricated WGM microlaser biosensors can detect human IgG at the concentration level of around 15.94 ag/mL. Such WGM microlaser sensors have advantages of small size, high sensitivity, and high level of integration and thus offer new opportunities for the development of future portable disease diagnostic devices.

Publications arising from the thesis

Journal papers:

1. **Z. Wang,** B. Zhou, and A. P. Zhang, "High-Q microcavity-based optofluidic biosensing technologies for biological analysis". (under review)
2. W. Hao, Y. Zhang, **Z. Wang**, and A. P. Zhang. "Directly printed plasmonic substrates of gold micro-flake array for plasmonically-enhanced infrared absorption-spectroscopic biodetection." *Sensors and Actuators B: Chemical*, Vol. 399, p.134841, 2024.

Conference papers:

1. **Z. Wang**, Y. Qin, and A. P. Zhang. "Optically 3D μ-printed directional-emission WGM microlasers for on-chip integrated sensing," *Conference on Lasers and Electro-Optics (CLEO) 2023*, ID: 3856081, San Jose, California, USA, 07–12 May 2023.
2. N. Wang, **Z. Wang**, B. Zhou, Y. Qin, and A. P. Zhang, "3D micro-printed Limacon-shaped whispering-gallery-mode microcavity for cavity-enhanced fluorescence spectroscopic sensing" *Optica Sensing Congress, Toulouse, France, 15 - 19 July, 2024*.

ACKNOWLEDGEMENTS

First of all, I would like to thank Prof. Zhang for providing me with the platform and his unfailing guidance throughout the program. I was impressed and benefited from his rigorous research attitude.

I wish to express my gratefulness to Dr. Bin Zhou for his indispensable help in the biosensing experiments and paper writing. Also, I would appreciate Mr. Yiang Qin and Mr. Nan Wang for their help in the experiments.

TABLE OF CONTENTS

Chapter 1. Introduction

1.1 Background

Optical sensors have shown their great promise in the applications of ultra-high sensitivity detection of biomolecules. The detection of biomolecules at a very low concentration in the human liquid samples such as serum may benefit the early diagnosis of diseases [1]. With the development of micro and nano technology, there are many micro and nano optical structures have been fabricated for ultra-sensitive detection in various fields, such as optical resonant microcavities [2], on-chip optical waveguides [3], optical fiber sensors [4] and so on.

Optical resonant microcavity, as demonstrated by Vahala's research team [5], is a kind of optical devices that can confine light wave in a small space for a relative long time. A very important parameter describing the quality of an optical microcavity is the quality (Q) factor. Generally, the higher the Q value of the microcavity, the stronger the ability of confining light wave for circulation. Therefore, with a high Q value optical microcavity, photons can be well confined within a small volume, which can greatly enhance the interaction between photons and matter. Optical microcavities have gained a wide range of applications, such as low-threshold lasers [6], nonlinear optics [7], high-sensitivity biodetection [8, 9] and many other biological applications that require a ultra-low limit of detection.

Optical whispering-gallery-mode (WGM) microcavities is a kind of optical resonant microcavities that are usually very small, in the order of a few light wavelengths. Materials commonly used to fabricate optical microcavities can be divided as organic polymers, such as SU-8 photoresists, and inorganic materials with high refractive index and low optical loss, such as Si, SiO_2, and lithium niobate. For different materials, researchers have developed different methods to perform the fabrication of WGM optical microcavities. For polymers, common

manufacturing technologies are usually single-photon exposure or two-photon polymerization technologies. The most common and simplest fabrication technique for the materials of glass is high-temperature fusion sintering. When dealing with Si and LiNb, the most common fabrication technique is photolithography plus etching with a highly corrosive gas or liquid [10].

Compared with other optical resonators, WGM microcavities are relatively easy to be fabricated and achieve a high Q value. Many researchers have already explored the applications of WGM microcavities in many different scenarios [10]. For instance, in the field of biomedical diagnostics, protein detection technology with extremely high sensitivity has very important practical applications [11]. Most diseases are expected to be diagnosed in early stages to prevent delaying necessary treatment which may lead to serious consequences. Indeed, most diseases, including cancers, produce extremely small amounts of characteristic proteins in the serum in the very early stage of development. Optical WGM microcavity sensors with extremely high detection sensitivity are very promising to achieve an ultra-low limit of detection of trace proteins in serum.

For a WGM microcavity, the binding of target molecules on its surface within the evanescent field may cause a splitting or shifting of its transmission spectrum (or emission spectrum for active WGM microcavity). It was demonstrated that, by detecting such splitting or shifting of the spectral peak, one can achieve the detection of nanoparticles [12]. In the biological field, single-molecule detection of macromolecular proteins by WGM microcavity sensor has been reported [13]. Moreover, the small size of WGM microcavity makes it easy to be integrated to manufacture portable bioassay devices. Most of the studies mentioned above use passive microcavities, which require a highly precision coupling system. The results are very sensitive to the relative position between the coupling optical fiber and WGM microcavity. A slight external perturbation may affect experimental results.

Such a problem can be alleviated by using WGM microcavity laser sensors instead of passive microcavities [14]. WGM microcavity lasers usually have a far-field emission pattern. Collecting the emitted light by using a far-field collection scheme can greatly reduce the influence of the relative positions between the coupling fiber and WGM microcavity on experimental results. Microlasers based on high-*Q* WGM optical microcavities often have very fine spectral lines. As a result, such microlaser sensors can achieve very low limit of detection in sensing molecules or micro/nano particles within their evanescent fields.

As a perfect rotational symmetry of the circular or spherical microcavity can easily form high-*Q* WGM modes, most of existing WGM microlaser sensors use circular or spherical microcavities [15]. However, WGM microlaser sensors made of such microcavities have also some obvious problems in practical application. One of the most important points is from its perfect rotational symmetry, which leads to an isotropic laser emission and makes the collection efficiency of the emitted light low. This means that a relatively high power of the pump light is needed to obtain a strong and stable optical spectral signal. As a strong pump light will do harm to the activity of biomolecules, it may lead to many practical issues in practical biodetection applications. To tackle such a problem, we will design and fabricate cavity-deformed WGM microlaser sensors for biodetection applications.

Regarding the fabrication of WGM microcavities, the commonly used technologies include droplet-based technologies, two photon polymerization, and electron-beam lithography. All these technologies can overcome the limitations of conventional lithography [16-20]. However, each of these technologies mentioned above has its own advantages and disadvantages. Droplet-based technology is quick and easy to apply, but it is difficult to control the geometry of the final microcavity. Thus, it is usually used to fabricate microcavities whose geometry is relatively simple such as microspheres. By contrast, electron-beam lithography can fabricate microstructures of various predesigned shapes. However, it lacks the ability of the fabrication

of 3D microcavity. On the other hand, two photon polymerizations can be used to flexibly fabricate 3D microcavity of arbitrary geometry. However, it need use a photoresist doped with efficient two-photon absorption dye and employs a single very small light spot to fabricate a 2D/3D microcavity in a scanning manner. Consequently, its fabrication process is usually very time consuming and expensive, which thus make the fabricated 3D microcavity sensors less competitive.

1.2 Research objectives

This project aims to develop cavity-deformed WGM microlaser biosensors for label-free biodetection. Through a careful design of weakly deformed optical WGM microcavities, WGM microcavity lasers can achieve a high Q value while maintaining good directional emission for far-field coupling of the laser signal and the optical fiber. A 3D micro-printing technology will be established to directly print the designed WGM microlaser biosensors. Thanks to the custom-built maskless UV exposure system, the entire microfabrication processes become very flexible and ease of use in the fabrication of weakly deformed WGM microcavity lasers. Experiments will be demonstrated to reveal the label-free biodetection ability of such high-sensitivity WGM microlaser sensors.

1.3 Outline of thesis

In this thesis, a kind of cavity-deformed WGM microlaser sensors is designed and numerically investigated. A UV optical maskless exposure system based on a spatial light modulator is applied to fabricate the designed WGM microcavity laser sensors. Such WGM microlaser sensors have been experimentally tested for high-sensitivity specific detection of protein molecules.

Chapter 2 will be an overview of microcavities and their applications in biological sensing. This chapter will be centered on different shapes of WGM microresonators. By showing the many studies that have been done combining microcavity and microfluidics, many recent advances and prospects in this field are presented.

Chapter 3 shows the numerical simulation and analysis of WGM microcavities of different shapes. Circular cavities, Limacon-shaped cavities, and elliptical cavities are compared by numerically analyzing their WGMs as well as from several angles such as ray simulation. These simulations illustrate the difference between a deformed cavity and a circular cavity, showing the reason why we chose deformed WGM cavity microlasers for biosensing.

Chapter 4 presents the details of the fabrication and testing of cavity-deformed WGM microlaser sensors. From WGM microcavities to WGM microlaser sensors, the detailed fabrication processes of 3D micro-printing of WGM microcavity laser sensors are described. The fabricated WGM microlasers have also been tested by using an own-established optical pumping test setup.

Chapter 5 focuses on bioassay experiments. This chapter describes the experimental process and results of the sensitivity test, and the processes and results about the use of WGM microlaser sensors on biomarker assay.

Chapter 6 is a summary of the whole project and an outlook on the future development of related technologies.

Chapter 2. Overview of WGM microcavity-based biosensors

2.1 Introduction

Optical microcavities are a kind of photonic devices that can tightly confine light for resonant circulation in a micrometer-scale volume [18]. It has become an indispensable platform for studying many intriguing optical processes, such as cavity quantum electrodynamics (QED) [19], optical chaos [20], nonlinear optics [21] and optical frequency comb generation [22]. As it can significantly enhance the interaction between light and matter, high-quality factor (Q) optical microcavities have attracted intensive attention in high-sensitivity sensing applications. Particularly, many designs of optical whispering-gallery mode (WGM) microcavities with high-Q factors and small mode volumes have been proposed for various kinds of biosensing applications. Optical WGM microcavities typically have a well-engineered boundary at which light is efficiently confined via a total internal reflection. Evanescent waves thereby exist beyond the boundary of optical WGM microcavities and exponentially decay in the radial direction. Correspondingly, optical WGM microcavities are highly sensitive to external perturbations and very suitable for ultrasensitive biosensing via evanescent waves. Optical WGM microcavity biosensors have the advantages of small size and high sensitivity and thus are very promising in the development of miniaturized biological analytical tools, such as integrated portable devices for point-of-care diagnostics.

However, there remain many challenges for optical WGM microcavity biosensors such as the ease of surface contamination and the requirement of surface functionalization. These shortages might be overcome by combination with another promising technology in biochemical analysis, i.e., microfluidic chip technology. It may pretreat liquid samples and

deliver liquids for not only functionalization but also detection in a fully automated manner. Moreover, it has the advantages of miniaturization, portability, reduced sample/reagent consumption, rapid analysis, high throughput and can be integrated with multiple functions. Therefore, the integration of optical microcavity sensors with microfluidic technology provides a great opportunity for development of innovative optofluidic devices benefiting from the advantages of both high-Q microcavities and microfluidic technologies in various kinds of biological applications [23-35].

Recently, various optical microcavity-based optofluidic technologies have been demonstrated for various biological applications, such as protein and nucleic acid detections, exosomes and virus analysis. They can acquire information about the type, concentration, and even the mass of biomarkers from very small amounts of serum and thus may enable the development of many innovative devices for biological detection. In this paper, we will review various integrated microfluidic chip technologies based on high-Q optical microcavities to demonstrate the exciting prospects of this technology in biological analysis.

2.2 Working principles of optical WGM microcavity biosensors

Optical WGM microcavities are an analogue to acoustic whispering gallery in which sound wave can travel along due to multiple reflections and can confine light for resonant circulation at the outer edge via total internal reflection. They are typically spherical or cylindrical structures made of low optical loss materials, such as silica, silicon nitride, and lithium niobite [22]. They can confine and accumulate light waves of specific wavelengths or frequencies satisfying the condition for constructive interference in WGM microcavities and thereby form very high-*Q* resonant modes, which results in long photon lifetime and strong light-matter interactions.

Generally, WGMs can be classified by using three mode indices, *i.e.*, azimuthal order *m*, radial order *s*, and polar order *l*, as well as their polarization, *i.e.*, transverse electric (TE) or transverse magnetic [23] polarized modes, in optical microcavities. If use a tapered optical microfiber or waveguide to couple with an optical WGM microcavity, one can obtain a transmission spectrum with a group of absorption tips that corresponds to WGMs at their resonant wavelengths. In general, these spectral peaks of WGMs exhibit a Lorentzian line shape that can be expressed as [24],

$$T(\omega) = a_i \frac{\left(\gamma_i / 2\right)^2}{\left(\omega - \omega_i\right)^2 + \left(\gamma_i / 2\right)^2} \tag{1.1}$$

where a_i is amplitude, ω_i is resonance frequency, and γ_i is the full-width at half maximum (FWHM) of the resonant frequency.

The essentially important parameter for a WGM is its quality factor, *i.e.*, the *Q* value. It describes the microcavity's ability in optical energy storage against optical power losses and reflects the average photon lifetime of a particular WGM in a microcavity. In general, the *Q* value of an optical microcavity can be calculated by

$$Q_i = \omega_i / \gamma_i \text{ (or } \lambda_i / \lambda_{FWHM}) \tag{1.2}$$

where λ_i is the resonant wavelength and λ_{FWHM} is the FWHM of the resonant wavelength. If the effective refractive index of a WGM is known as n_{eff}, the free spectral range (FSR) between transmission tips, i.e., between a WGM and its neighboring mode, of a circular WGM microcavity in terms of frequency (or wavelength) is

$$\Delta f_{FSR} = \frac{c}{2\pi n_{eff} R} \text{ (or } \Delta\lambda_{FSR} = \frac{\lambda^2}{2\pi n_{eff} R}) \tag{1.3}$$

where c is the speed of light in vacuum, and R is the radius of the circular WGM microcavity. In sensing applications, the ratio of FSR and FWHM defines another important figure of merit, i.e., finesse (F) of a WGM microcavity as $F=\lambda_{FSR}/\lambda_{FWHM}$.

WGM microcavities have been widely considered as promising sensors for ultrasensitive detection of biomolecules in microfluidic environments and systems. When target molecules, such as proteins, approach the surface of a WGM microcavity, it will cause an excess dipole moment via the evanescent field of WGMs. Consequently, the resonant frequency of WGMs will shift which can be evaluated by an integral over surface differentials [25]

$$\frac{\delta\omega_i}{\omega_i} \approx -\frac{\alpha_{ex}\sigma_m}{2\varepsilon_c}\frac{\int\left|\mathbf{E}_i(\mathbf{r})\right|^2 dA}{\int\left|\mathbf{E}_i(\mathbf{r})\right|^2 dV} \tag{1.4}$$

where α_{ex} is the molecule-caused excess polarizability, σ_m is the molecular surface density, ε_c is the homogeneous permittivity of the WGM microcavity and $\mathbf{E}_i$ is the electric field of the WGM.

Recently, active WGM microcavities made of an active material and working as a micrometer-scale laser sources have attracted great attention in biosensing applications because of their distinct far-field light coupling ability. For such WGM microlaser sensors, one can use not only the resonant frequency but also the intensity of laser output for various kinds of biosensing schemes, such as on-chip optofluidic enzyme-linked immunosorbent assay (ELISA). If considering the bio-reaction induced optical loss around a WGM microlaser sensor, the relation between the intensity of laser output and the bio-reaction induced optical losses can be expressed as [26]

$$I_{Laser} \propto I_{pump}\delta_c\left(\frac{g}{\delta_c + c_a\delta_{in} + c_b\delta_{ex}} - 1\right) \tag{1.5}$$

where I_{pump}, g, δ_c, δ_{in} and δ_{ex} are the intensity of pumping laser, the gain coefficient of WGM microlaser, the coefficients of external coupling, intrinsic and external optical losses, respectively. c_a and c_b are the coefficients depending on WGM distribution. Both active and passive WGM microcavities have become powerful building blocks in the development of high-performance integrated photonic devices and microsystems for biological applications.

2.3 Overview of High-Q microcavity-based optofluidics for biological applications

2.3.1 High-Q microcavity-based biosensors

With the development of high-Q optical microcavities, particularly WGM microcavities, many new optofluidic technologies and microsystems have been demonstrated for various kinds of biological analysis applications, as shown in **Fig**. 1. Micro-sphere cavity, micro-toroidal cavity and so on based optofluidic biosensing have been mentioned.

- **Micro-sphere cavity based optofluidic biosensors**

Microsphere cavities are the widely used structure for biosensing due to their ease of fabrication and achievable high-Q values. An early work about microsphere cavity-based optofluidic biodetection was demonstrated by V.R. Dantham et al. [27]. With a microsphere cavity, they reported the detection and sizing of the smallest individual RNA virus, MS_2, in which a single dipole stimulated plasmonic-nanoshell is adopted as a microcavity wavelength shift enhancer. Their experiments showed that such an enhancement mechanism allows an ultrasensitive detection of MS_2 viruses with a modest hybrid mode. An analytical theory for the dipole plasmonic enhancement with plasmonic nanoshell has also been presented together with experimental results. The demonstrated technology may enable early detection of viruses

at ultra-low concentrations for identification and elimination of pathogens.

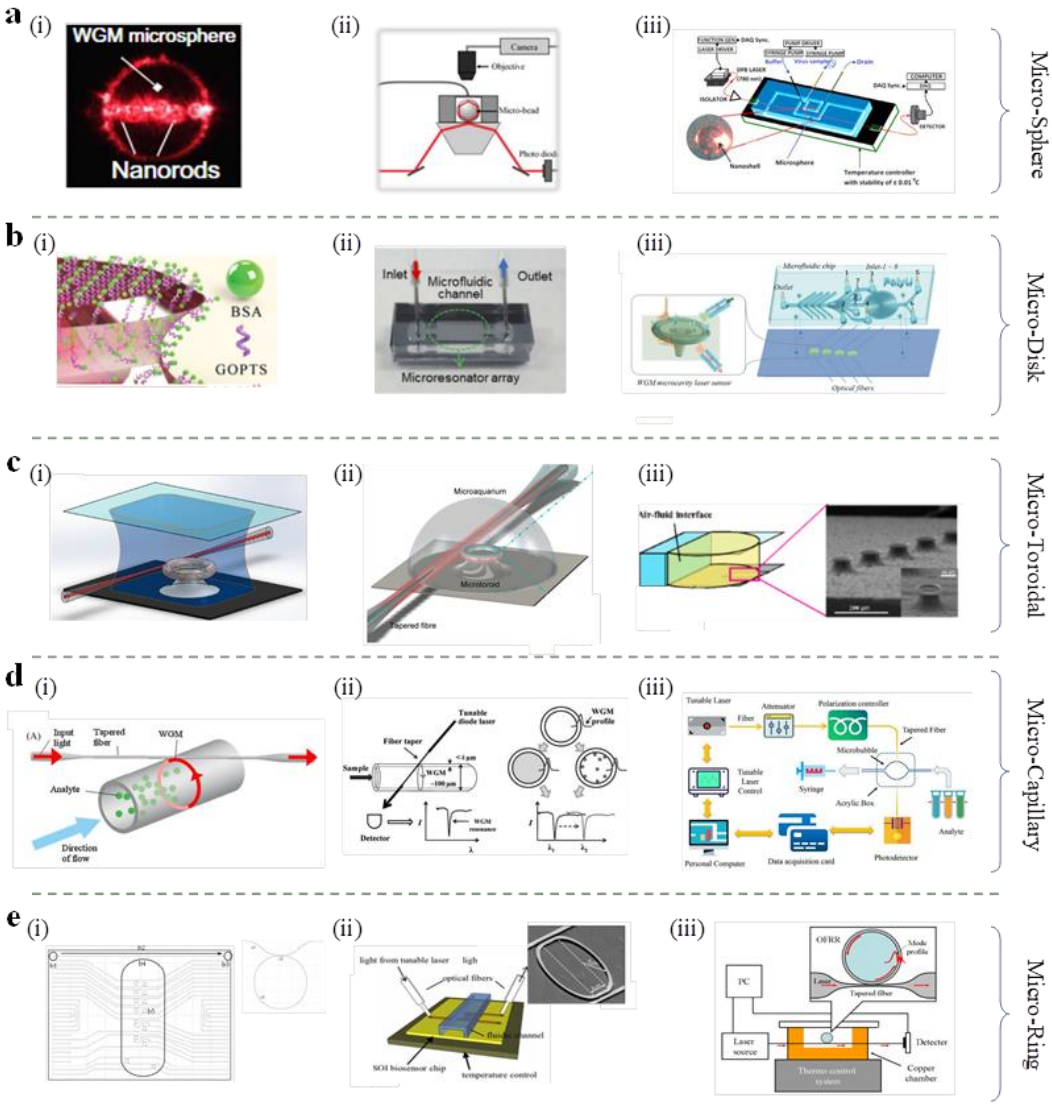

Figure 1. Different types of high-Q optical microcavity sensors for optofluidic biological analysis applications. a. Micro-sphere microcavity sensors for (i) monitoring polymerase/DNA interactions [22], (ii) label-free and real time detection of protein secretion [23], (iii) label-free detection and sizing of the smallest individual RNA virus [12]. b. Micro-disk microcavity sensors for (i) label-free detection of human IgG [24], (ii) label-free biosensing [25], (iii) label-free detection of human IgG [21]. c. Micro-toroidal microcavity sensors for (i) detection of human chorionic gonadotropin [26], (ii) selective biosensing without compromising sensitivity or reliability [27], (iii) investigation of the delivery of analytes [28]. d. Micro-capillary microcavity sensors for (i) detection of the HER2 breast cancer biomarker [29], (ii) sensitive label-free detection of viral (M13) [30], (iii) ultra-sensitive detection of lead ion [31]. e. Micro-ring microcavity sensors for (i) integration into a self-contained microfluidic cartridge [38], (ii) label-free real-time biosensing [19], and (iii) sensors within poly-(dimethylsiloxane) microfluidic channels [32].

Another method for label-free optical detection of single enzyme-reactant interactions and associated conformational changes at a single-molecule level was demonstrated by Eugene Kim et al. [28]. They used plasmonic nanorods and WGM microsphere cavity coupled device to monitor polymerase/DNA interactions. Two different recognition schemes, i.e., probe both the kinetics of polymerase/DNA interactions and the conformational changes in the polymerase molecules, were utilized in their experiments. Low and high polymerase activities were clearly discerned through their characteristic signal amplitude and signal length distributions. Their work established a promising label-free method for investigating structural changes in single molecules.

To overcome the limitations of existing methods for monitoring cell death and protein release, such as the requirements for cell labeling or protein purification, Y. Chen et al. proposed an optofluidic solution to use WGM microsphere microcavities for label-free specific detection of cytochrome c, a biomarker for cell apoptosis [29]. They demonstrated the immobilization of antibodies on the surface of WGM microcavity sensors using a sandwich assay with biotin-streptavidin linking. Microfluidic components were integrated for precise continuous flow control and mixing. Such an integrated optofluidic platform provided a label-free real-time detection technology for monitoring proteins released from cells at nM concentration level.

- **Micro-disk cavity based optofluidic biosensors**

Another common structure of WGM microcavity is micro-disk cavity, which can be regarded as the equatorial plane sliced from a microsphere cavity. Compared to microspheres, the generation of spurious WGMs can be efficiently suppressed because the thickness of micro-disk cavities is much thinner. Micro-disk WGM microcavities have also been widely combined with microfluidics for bioassays. Researchers from Canada used micro-disk WGM cavities as biosensors for real-time detection of Staphylococcus aureus [30]. A phage protein LysK, who

is specific for staphylococci, is used to functionalize these WGM microcavities. The binding event on the surface of WGM cavities caused a shift of resonant spectral peaks. The limit of detection (LOD) of such a microdisk sensor is 5 $pg \cdot mL^{-1}$, which corresponds to 20 cells per mL. The specificity of the functionalization scheme was verified via a control testing of detection of Escherichia coli. Although this technique has a simple structure and high sensitivity, optical coupling with the microcavity using tapered optical fiber is susceptible to environmental perturbations.

Such optical coupling-caused issues can be alleviated by transforming passive WGM microcavities to WGM microlasers, and therefore far-field coupling using optical fiber or objective lens can be applied to collect laser output for biosensing applications. For instance, Z. Guo *et al.* demonstrated a hyperboloid-drum (HD) micro-disk WGM microlaser biosensor for ultrasensitive detection of human IgG [31]. Notably, such a HD micro-disk WGM microlaser biosensor showed an impressive LOD of 9 ag/mL in the detection of human IgG, which is approximately four orders of magnitude more sensitive than typical WGM biosensors. Their experimental results also showed that the WGM microlaser biosensors are promising in the detection of biomarkers in protein secretions or body fluids.

Y. Kim *et al.* proposed an on-chip label-free biosensor based on active WGM sensor using silicon nanoclusters as a stable active compound [32]. The authors introduced a nano-gap structure in WGM microresonators to enhance sensitivity. The fabricated sensors were integrated within a microfluidic channel, forming a compact optofluidic device. The optical responses of the active WGM sensors were tested in both air and aqueous conditions, which showed strong photoluminescence emission with WGM microcavity resonances. They also demonstrate a platform operating with a remote pump and readout that reduced the complexity and cost of the measurement setup.

M. Goede *et al.* fabricated a microdisk WGM laser biosensor using Al_2O_3 doped with Yb^{3+}

because it has low optical losses and can emit light in the range 1020 ~ 1050 nm that is outside the absorption band of water [33]. Their fabricated WGM microlaser can achieve single-mode emission at the wavelength of 1024 nm and its linewidth is about 250 kHz. An LOD of 300 pM was achieved in the detection of the protein rhS100A4 in urine. Their work revealed the advantages of WGM microlaser-based biosensors, particularly the WGM microlaser sensors fabricated by using Al_2O_3, over passive WGM sensors.

X. Ouyang *et al.* demonstrated an optofluidic ELISA by using on-chip integrated polymer WGM microlaser sensors [26]. They used an optical 3D μ-printing technology to rapidly fabricate high-*Q* suspended-disk WGM microlaser sensors and then integrate them together with optical fibers upon a microfluidic chip. The use of high-*Q* WGM microlasers in optofluidic ELISA offers advantages such as low-threshold laser oscillation and strong light-matter interactions. Such an on-chip WGM microlaser-based optofluidic ELISA technique can detect vascular endothelial growth factor (VEGF) at the concentration level of 17.8 $fg \cdot mL^{-1}$, significantly surpassing the capability of conventional ELISA kits.

- **Micro-toroidal cavity based optofluidic biosensors**

Micro-toroidal is a structure like micro-disk but has a smooth ring around the edge. Compared to micro-disk, micro-toroidal shaped microcavities usually could achieve higher *Q* value and thus may obtain better biosensing performance in terms of sensing sensitivity and LOD.

Using micro-toroidal microcavity, E. Ozgur *et al.* proposed a highly sensitive biosensor for rapidly detecting the performance-enhancing drug human chorionic gonadotropin (hCG) in urine samples [34]. They used frequency locked microtoroid WGM resonators as biosensors that can detect hCG at concentrations of 1 fM in simulated urine and 3 fM in the urine of pregnant donors. It was three orders of magnitude better than mass spectrometry, which is the current gold standard of detection, in terms of LOD. E. Ozgur *et al.* proposed a surface modification strategy using a silane-based coating that is both protein resistant and

bioconjugable, enabling highly selective biosensing without compromising sensitivity or reliability [35]. The strategy is demonstrated using functionalized microtoroids, which resist nonspecific interactions while being used as sensitive biological sensors.

Recently, S. Suebka *et al.* constructed a micro-toroid optical resonator-based biosensor. In this work, the researchers investigated the best way to deliver the analyte to the surface of WGM microcavities integrated on an optical microfluidic chip biosensor from two perspectives: simulation very experimental [36]. They found that continuous injection is the fastest way to deliver the analyte. The result gives insights into the mass transport mechanisms and optimize sensor performance.

- **Micro-capillary/micro-bubble cavity based optofluidic biosensors**

Another commonly used structure is the capillary, which is a very clever combination of microfluidic and WGMs**.** This scheme has a simple structure and directly utilizes the capillary wall to form the WG pattern. Then a liquid is passed through the inner wall of the capillary to realize the interaction of biomolecules and ms with each other. Y. Wang *et al.* presented a capillary-based microfluidic WGM microresonator for real-time monitoring of the conformational change of G-quadruplex driven by K^+ ions [37]. The resonance wavelength shift mechanism is analyzed theoretically, and the resonance mode with the largest wavelength sensitivity is selected for monitoring. Experimental results confirm the theoretical analysis and show that G-quadruplex can be folded with a *KCl* concentration down to 1 μM. The proposed microresonator-based platform offers high sensitivity, integration, microfluidic capability, label-free detection, and real-time monitoring, making it suitable for DNA sensing and other applications. The document also provides details on the materials and methods used in the experiment.

J. Sutera et al. and H. Zhu *et al.* respectively proposed structures for biosensing using capillary tubes combined with WGM. They discussed the use of the liquid core optical ring

resonator (LCORR) sensor for label-free quantitative DNA and viral detection [38, 39]. The LCORR is a sensing platform that integrates microfluidics and photonic sensing technology, allowing for low detection limits and sub-nanoliter detection volume. The researchers analyzed the LCORR response to different DNA and viral samples with varying strand lengths, number of base-mismatches, and concentrations to evaluate its detection capability. They established a linear correlation between the LCORR sensing signal and the molecule density, allowing for accurate calculation of the molecule density on the surface. The researchers also demonstrated that the LCORR was sensitive enough to differentiate DNA and viral with only a few base-mismatches.

To make the evanescent field inside the tube stronger and to enhance the interaction between the WGMs and the biomolecules, one option that can be taken is to fabricate a micro-bubble based on a capillary tube using, for example, heating. Micro-bubbles have a thinner wall and will thus leak more energy inside the bubble in forms of evanescent field when the WGM operates within the wall. Liang Fu *et al.* proposed a ultrasensitive method for detection of lead ion using a microbubble-based WGM optofluidic resonator sensor [40]. Lead ions are harmful pollutants that can contaminate drinking water and pose health risks, especially to children. The proposed method involves modifying the inner wall of a microbubble with classic GR-5 DNAzyme and analyzing the mode field distribution of the microbubble. The optofluidic sensor exhibits a high bulk refractive index sensitivity and can detect lead ions at concentrations as low as 15 fM. The sensor showed good selectivity in detection of lead ions over other metal ions. The experimental setup and fabrication process of the microbubble resonator are described in detail. The proposed sensor has potential applications in environmental monitoring and food safety analysis. Recently, a novel label-free DNA biosensor based on a high-quality optical WGM microcavity modified with 3D DNA nanostructure probes was designed by H. Wan *et al.* [41]. The biosensor achieved an ultra-low LOD by

modifying the surface of the microcavity with DNA tetrahedral nanostructure (DTN) probes. The DTN probes can efficiently improve probe density and depress the entanglement between DNA probes, which resulted in a 1000-times lower LOD compared to that achieved by using 1D ssDNA probes. The WGM spectra of high-Q microcavity was employed to detect DNA inside the microfluidic channel. The proposed biosensor has broad application prospects in bioengineering and medical diagnosis.

- **Micro-ring cavity based optofluidic biosensors**

Micro-ring cavities are a kind of increasingly important WGM resonators that are very suitable for on-chip integrated optofluidic biosensing. As early as 2007, K. Vos et al. proposed a label-free biosensor based on microring cavities in silicon-on-insulator (SOI) for sensitive and real-time biosensing [18]. The biosensor is designed to overcome the limitations of commercialized microarrays that rely on the detection of labeled molecules. In their research, they utilized microring cavity resonates at a specific wavelength, and any change in the refractive index of the cavity's environment causes a shift in the resonance spectrum, which can be monitored for sensing. The device performs well in terms of absolute molecular mass sensing due to its small dimensions. The biosensor is fabricated using deep UV lithography, allowing for cheap mass production and integration with electronic functions for complete lab-on-chip devices.

S. Geidel *et al.* demonstrated an optofluidic biochip by integrating optical ring resonator biosensors into a self-contained microfluidic cartridge with active, single-shot micropumps [42]. The microfluidic cartridge was designed to include multiple reservoirs for reagent storage and single-use electrochemical pumps for time-controlled delivery of liquids. Their optofluidic biochip successfully performed an immunoassay but with relatively low sensitivity. Nevertheless, their work showed the importance of automation and miniaturization in optofluidic biochemical analyses and revealed the advantages of photonic microsystems in

biosensing. Moreover, S. Wu *et al.* presented the design, fabrication, and characterization of an optofluidic chip by integrating highly sensitive, label-free microring optical resonator sensors within poly-(dimethylsiloxane) microfluidic channels [43]. Such a microring resonator-based optofluidic chip was capable of real-time, quantitative detection of biomolecules and has great potential applications in environmental monitoring and medical diagnostics.

A summary of different microcavity-based optofluidic technologies for biological analysis is presented in Table 1.

TABLE 1. Comparison between different microcavity-based optofluidic sensing technologies.

Structure	Principal	Target biomarkers	LOD	References
Micro-Sphere	Plasmonic enhanced mode shift	Smallest individual RNA virus MS2.	Individual virus (6 ag)	[27]
	Binding-induced linewidth broadening and wavelength shifts	Polymerase/DNA interactions	Single-molecule level	[28]
	Mode shift	Cytochrome C	6.82×10^{-9} M	[29]
Micro-Disk	Enzyme-linked immunosorbent assay (ELISA) using light intensity of active WGMs	Horseradish peroxidase (HRP)-streptavidin; Vascular endothelial growth factor (VEGF)	0.3 ng/mL and 17.8 fg/mL	[26]
	Mode shift of active microcavity	Human IgG	9 ag/mL (0.06 aM)	[31]
	Mode shift of active microcavity	Streptavidin-biotin complex	6.7 nM	[32]
	Mode shift of WGM microlaser	Protein rhS100A4 in urine	300 pM (3.6 ng/mL)	[33]
Micro-Toroidal	Mode shift of passive microcavity	Human chorionic gonadotropin (hCG)	120 aM	[34]
	Mode shift caused by adsorption events	Human IL-2 protein	0.3 fM	[35]
Micro-Capillary	Blue spectral shift of WGMs	(Potassium chloride) KCl	1 μM	[37]
	Mode shift of passive microcavity	Lead ions	15 fM	[40]
	Mode shift in real time	DNA	260 aM	[41]
	Mode shift	Filamentous bacteriophage M13 virus	2.3×10^3 pfu/mL	[44]
	Mode shift of WGMs and enzyme-linked immunosorbent assay (ELISA)	HER2 extra-cellular domain breast cancer biomarker	100 ng/mL	[45]
	Mode shift	Biotin	10 nM	[46]
Micro-Ring	Mode shift	Avidin/biotin high affinity couple	10 ng/ml	[23]
	Mode shift	Bulk DNA	10 pM	[38]
	Mode shift	DNA	4 pg/mm^2	[35]

	Mode shift	Human IgG	0.5 μg/ml	[36]
	Mode shift	Avidin	0.1 nM	[47]

2.3.2 Biological analysis applications

Optical microcavity-based optofluidics have become one of the most promising technologies in ultrasensitive biological analysis applications. They have many distinct advantages, such as minimal sample requirements, ease of integration, high sensitivity, and rapid detection abilities. It was reported that they can be very sensitive to even measure single particles [48] and have been demonstrated for many different kinds of biological analyses, such as protein, nucleic acid, exosomes and viruses detections as well as cell studies.

A. Protein studies

Optical WGM biosensors have shown their remarkable performances in detection of proteins. F. Vollmer *et al*. demonstrated the first use of an optical WGM biosensor in detecting protein, i.e., bovine serum albumin (BSA), in 2002 [49]. Thereafter, J. Gohring *et al*. presented an optofluidic ring resonator (OFRR) sensor for detection of human epidermal growth factor receptor 2 (HER2) breast cancer biomarkers in human serum samples. In their experiments, OFRR sensors can detect HER2 at concentrations of 13 to 100 $ng \cdot mL^{-1}$ [50]. With a directly printing polymer WGM microlaser biosensor, X. Ouyang *et al*. demonstrated an optofluidic ELISA technology that can measure horseradish peroxidase (HRP)–streptavidin at the concentration level of 0.3 $ng \cdot mL^{-1}$ and detect vascular endothelial growth factor (VEGF) at the concentration level of about 18 $fg \cdot mL^{-1}$, far exceeding commercial ELISA detection capability in the market at the time. Notably, using a hybrid microcavity of optical WGMs and plasmonic nanoshell, V. Dantham *et al*. presented an ultrasensitive biosensor that can detect single thyroid

cancer marker (Thyroglobulin, Tg) with a mass of only 1 ag. Its LOD in detecting the mass of BSA protein reached 0.11 ag (66 kDa) [51].

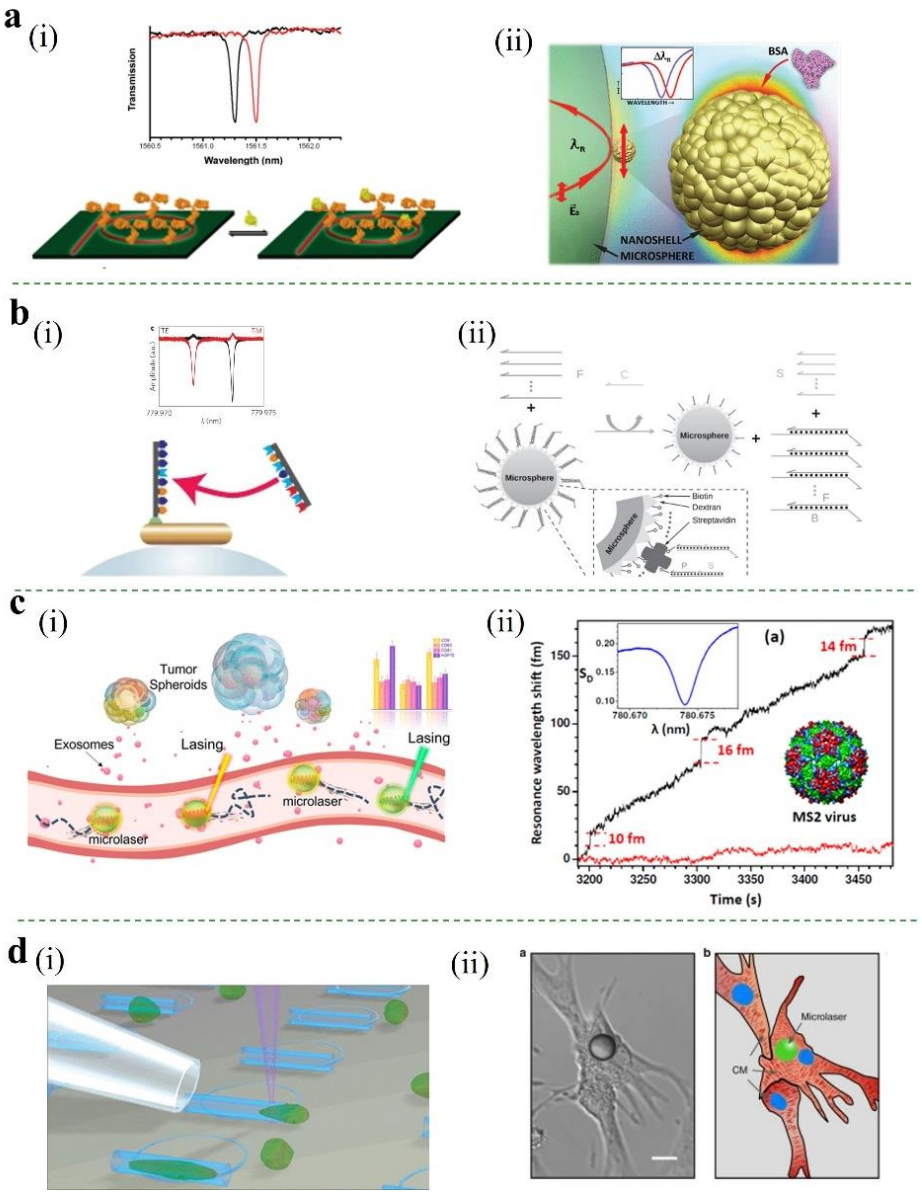

Figure 2. Biological analysis applications of optical microcavity-based optofluidic technologies. a. Protein study: (i) detection of proteins [7], (ii) single protein detection [45]. b. DNA study: (i) on-chip DNA analysis [52], (ii) analysis of DNA molecules [50]. c. Exosome and virus detections: (i) Detection of released extracellular vesicles [57], (ii) Detection of MS2 viruses [12]. d. Cell study: (i) detection of individual mouse cells [58], (ii) study of cardiomyocytes [49].

Protein detection using WGM microcavity sensors can be performed very quickly. For instance, J. Gohring *et al.* reported that the detection time can be reduced to 30 min by using optical microcavity sensors [50]. Moreover, the integration with microfluidics can enable microcavity sensor system with high throughput in the detection of multiple proteins [52]. As the inherent complexity of biochemical pathways always alters disease states, it is thus highly demanded to use multiplexed analytical technology with more informative biomolecular understandings of disease onset and progression. Compared to conventional single-parameter assays, biomolecular insight gleaned from multiparameter measurements may greatly improve disease diagnostics, prognostics, and theragnostic. A. L. Washburn *et al.* demonstrated that the concentrations of prostate specific antigen (PSA), alpha-fetoprotein (AFP), carcinoembryonic antigen [19], tumor necrosis factor-alpha (TNF-alpha), and interleukin-8 (11,8) can be simultaneously determined in three unknown protein cocktail solutions [52]. Their work revealed that multiple immunoassays can be performed concurrently on a WGM biosensor-based optofluidic platform without loss of sensitivity or measurement precision.

B. Nucleic acid studies

Detecting nucleic acids, including various types of deoxyribonucleic acid (DNA) and ribonucleic acid (RNA) molecules, with WGM microcavity sensors has also been widely reported [53-57]. Most measurement strategies investigated the hybridization of complementary nucleic acid strands, and their key measurement considerations include sensitivity, the capability to detect subtle discrepancies such as single-base mismatches, and response time.

Nucleic acid detection using WGM microcavity biosensors can avoid the use of costly fluorophore functionalization steps in conventional assays and achieve ultimate low limit of detection. For instance, Y. Wu *et al.* demonstrated a microsphere-type WGM biosensor which can detect a 22nt oligomer at the concentration of 80 pM (i.e., 32 fmol) [56]. A DNA strand

displacement circuit is integrated with WGM microsensor for nucleic acid detection, in which the catalytic behavior of the circuit can not only improve its sensitivity and specificity, but also make the sensor reusable. M.D. Baaske *et al.* proposed a microsphere-type WGM microcavity biosensor platform to monitor single-molecule nucleic acid interactions [58]. With plasmonic enhancement using gold nanorods, such a biosensor can specifically detect nucleic acid hybridization down to single 8-mer oligonucleotides.

C. Exosome and virus detections

To contain the infection and prevent pandemic outbreaks, rapid and accurate detection of viruses have become increasingly important. Likewise, detection of exosomes, which are small particles secreted by cancer cells, has also drawn great attention for studying molecular information about tumors. Conventionally, their biological specimens need profiled by molecular biology techniques such as polymerase chain reaction (PCR). However, such techniques require extensive sample preparation and processing and may take several hours to complete. Recently, label-free optical microcavity biosensors have become a very promising candidate to revolutionize the technologies for exosome and virus detection.

In 2008, F. Vollmer *et al*. reported a WGM biosensor for detection of a single discrete binding event of influenza A (InfA) virus [59]. By monitoring the shift of resonance frequency/wavelength, the size and mass (about 0.52 fg) of a bound virion are determined from the measured resonance shift. T. Lu *et al*. demonstrated an optical WGM microcavity biosensor platform conjunct with a thermal-stabilized reference interferometer for detection of nanoparticle and virus [60]. Their system can detect InfA virus binding at a concentration of 1 pM, and its signal-to-noise was enhanced from the previously reported 3∶1 to 38:1. The detection of very small virus was reported by V. R. Dantham *et al*. [61]. They demonstrated that the use of a WGM microcavity sensor can enable the label-free detection and sizing of the

smallest individual RNA virus, i.e., MS2 virus, whose mass is only ~1% of Influenza A (6 vs. 512 ag).

Remarkable progresses have also been achieved in the detection of exosomes [62]. For instance, Z. Wang *et al*. proposed a liquid crystal microdroplet-based smart WGM microlaser sensor that can self-propel and analyze extracellular biomarkers [63]. Lasing spectral responses of such WGM microlaser sensors were employed to monitor cellular profiling of exosomes that were derived from multicellular cancer spheroids. The sensing capability of such WGM sensors in complex environments was tested by using a microfluidic biosystem with different tumor-derived exosomes.

D. Cell study

WGM sensors have also been employed to investigate the behaviors of individual cells, which are the fundamental structural and functional units of living organisms, and have potential to play an increasingly important role in the studies of cell biology, material-cell interactions, and biophysics. For instance, J.S. Elliot et al. reported a method for efficient capturing and sensing of embryonic fibroblast mouse cells (NIH 3T3) using split-wall microtube WGM resonators [64]. M. Schubert *et al*. introduced WGM microlaser sensors into cardiac cells to illuminate cardiomyocyte contractility under various experimental conditions [55]. Because of their single-cell specificity, long-term tracking, and reduced sensitivity to scattering, such WGM microlaser sensors can reduce complexity and experimental restrictions and offer new technological means far beyond current microscopy-based techniques.

2.4 Summary

In short, high-*Q* optical microcavity-based biosensing technologies have become an increasingly important technology in various kinds of biological analysis applications. WGM

microcavity sensors can be made into many different shapes, such as micro-spheres, micro-disks, micro-toroidal, micro-capillary/bubble, or micro-rings, and thus provide a group of very flexible technological means to enhance light-matter interactions for ultrasensitive biological study and biodetection applications.

After further combining high-*Q* optical microcavities with microfluidic technology, one may develop many kinds of small-size high-performance optofluidic biosensors to address many of currently pressing biological analysis challenges. They can be used to develop portable point-of-care testing and diagnostic tools for rapid and accurate detection of proteins, nucleic acids, viruses, or exosomes, which are highly demanded to tackle public healthcare challenges such as COVID-19 pandemic. They can also be employed to study the behaviors of living cells of human organisms, which may pave new pathways for the studies of cell biology and biophysics.

Chapter 3. Sensitivity analysis and optimization of cavity-deformed WGM microlaser sensors

3.1 Introduction

Most of the previous microcavity optical sensors utilize circular optical microcavities as the core component. Due to its perfect center symmetry, a circular microcavity usually achieves a high Q value. However, also due to its perfect central symmetry, its signal emission is isotropic, which provides a greater difficulty in coupling the microcavities to the waveguide. The conventional design uses optical fibers with diameters less than 2μm to approach the microcavity. This system is extremely demanding in terms of the relative position of the fiber and the microcavity and is very sensitive to external infections.

One of potential solutions to solve this problem is to use weakly deformed microcavities instead of circular microcavities. Weakly deformed microcavity can achieve directional emission of the signal while guaranteeing a high Q so that the signal can be coupled directly into the optical fiber. There have been a considerable number of papers discussing the directionality of deformed microcavities [65-67]. But how to achieve an ideal directionality while maintaining a high Q factor still needs systematic research and design. Here we have analyzed and designed the sensitivity to change of the refractive index of the host medium and the directionality of different types of deformed microcavities.

To understand optical responses of such deformed WGM microcavities and their sensitivities in label-free biodetection, we have conducted numerical simulations to analyze the distribution of WGMs of different designs of microcavities. A deformed microcavity combining high Q and

directional emission is designed by comparing the degree of symmetry breaking of WGMs in the microcavity under different shapes.

3.2 Simulation of transverse optical modes of circular WGM microcavities

In order to investigate the effect of deformation on the WGM distribution as well as the evanescent wave outside the microcavity, we first simulated the WGM distribution as well as the evanescent wave distribution at different diameters using COMSOL Multiphysics.

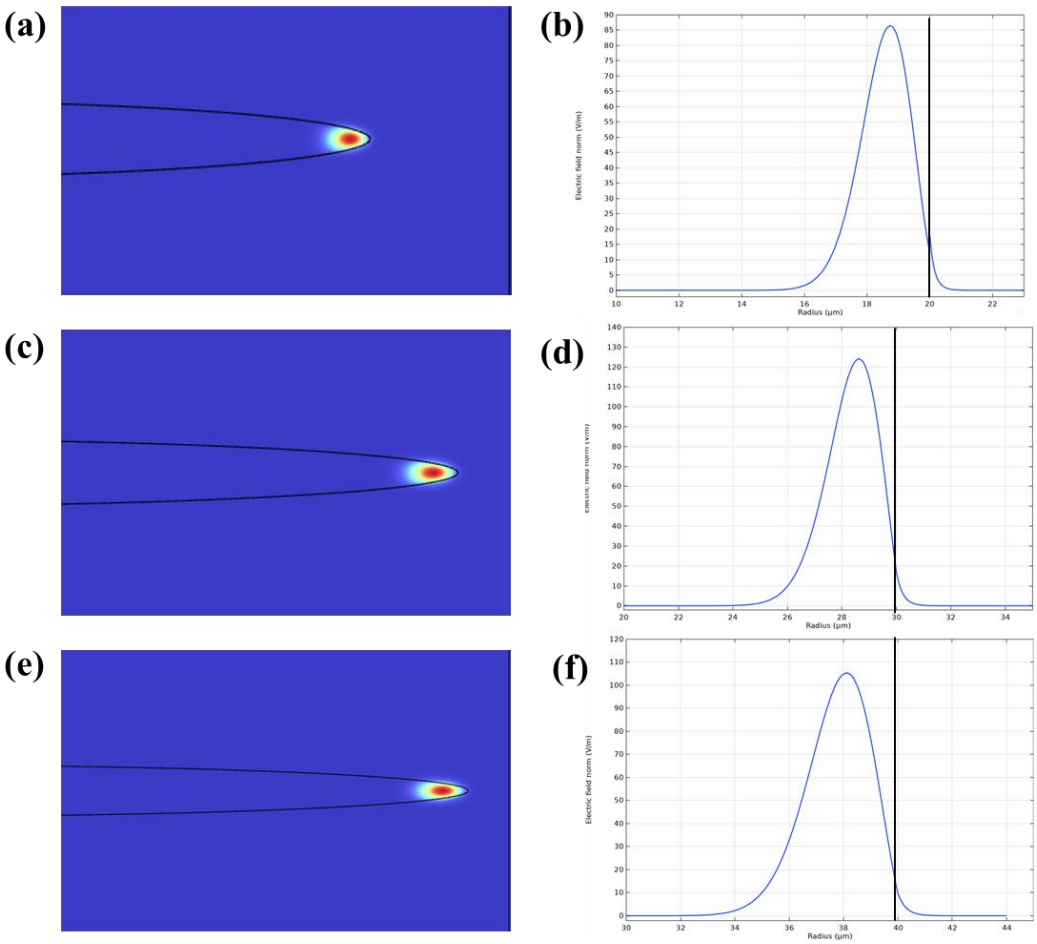

Figure 3. Simulated WGMs and their evanescent field distributions in the microcavities of different radius.

Radii of a microcavity (μm)	Azimuthal mode number	Percentage of the evanescent wave energy
55	950	1.15%
58		1.06%
60		1.01%

Table 2 Simulated energy percentages of the evanescent waves in different sized microcavities.

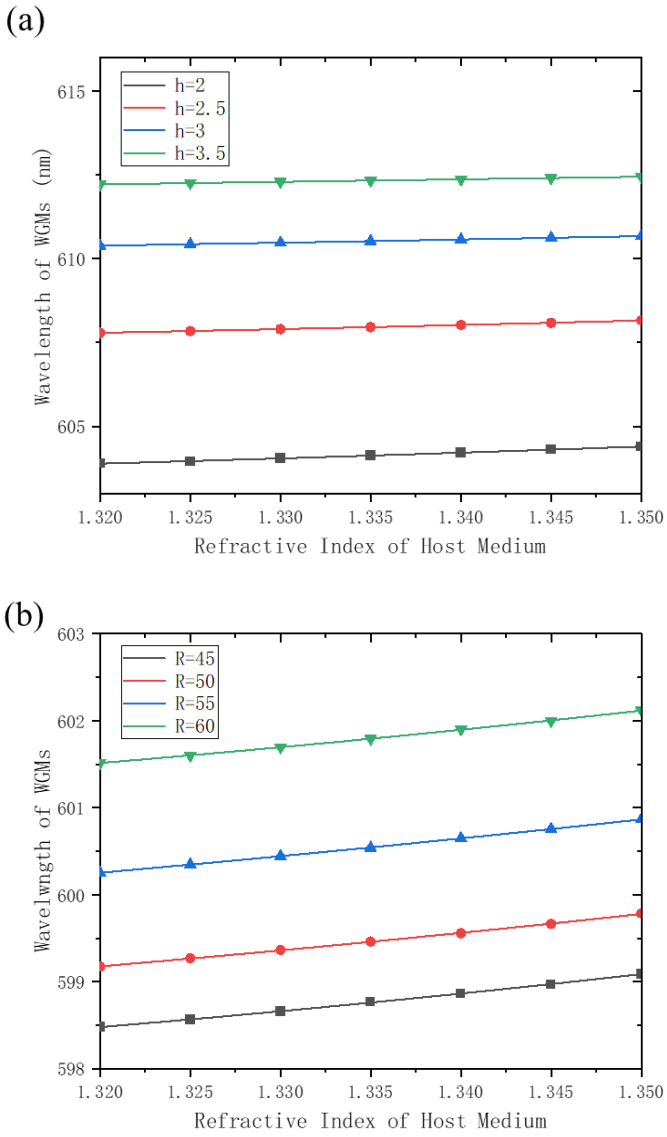

Figure 4. (a) Simulated wavelengths of the WGM microcavities of different thicknesses with respect to the change of external refractive index; (b) Simulated wavelengths of the WGM microcavities of different radiuses with respect to the change of external refractive index.

The results in **Fig**. 3 and **Table**. 2 show that, within a certain range, the smaller diameter of a microcavity is, the higher percentage of the evanescent wave energy is. The stronger evanescent wave energy means that at the surface of the microcavity, the WGMs and biomolecules could interact more strongly, which can lead to higher sensing sensitivity of the microlaser.

The results of the simulation of the relationship between wavelength of WGMs, thickness/radius of microcavity, and refractive index of host medium in a circular microcavity using Comsol Multiphysics are shown in **Fig**. 4. From **Fig**. 4 we can see that the thickness and radius changes of the microcavity weakly affect the sensitivity of the WGMs of microcavity.

Refractive Index of Su-8	Refractive Index of Host Medium
1.57	1.320
	1.325
	1.330
	1.335
	1.340
	1.345
	1.350

Table 3. Parameters for numerical simulation.

The parameters used for the simulation are shown in Table 3, the material of the microcavity was SU-8 and the refractive index was taken as 1.57. The refractive index of host medium was taken uniformly from 1.320 to 1.350.

3.3 Sensitivity analysis of weakly deformed WGM microcavity sensors

In order to facilitate the subsequent fabrication, we need to choose the weakly deformed microcavities with smooth contours for the study. Here we choose a so-called 'Limacon' shaped microcavity as well as an elliptical microcavity for our studies.

3.3.1 Sensitivity analysis of Limacon-shaped WGM microcavity sensors

The Limacon shape is defined as

$$\rho = R \cdot (1 + \varepsilon \cdot \cos\theta) \tag{1.3}$$

where $\varepsilon \in [0,1]$ represents the coefficient of deformation of the microcavity.

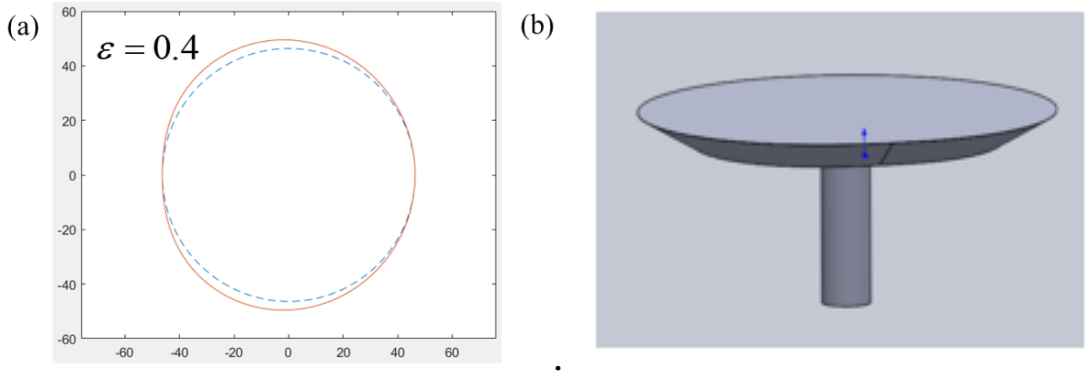

Figure 5. (a) Schematic of a Limacon-shaped cavity and (b) the 3D model of Limacon-shaped suspended-disk WGM microcavity.

Figure 5(a) is a schematic representation of Limacon cavity, whose rotational symmetry has been broken. Compared to a circular microcavity, the contour of the Limacon-shaped cavity has larger curvature radius at some positions and smaller curvature radius at the other positions. Besides, **Fig**. 5(a) shows that the contour of the Limacon-shaped microcavity with a deformation coefficient of 0.4 is close to that of circular microcavity. **Fig.** 5(b) shows the 3D model of a Limacon-shaped suspended-microdisk WGM cavity that we generated using Solidworks.

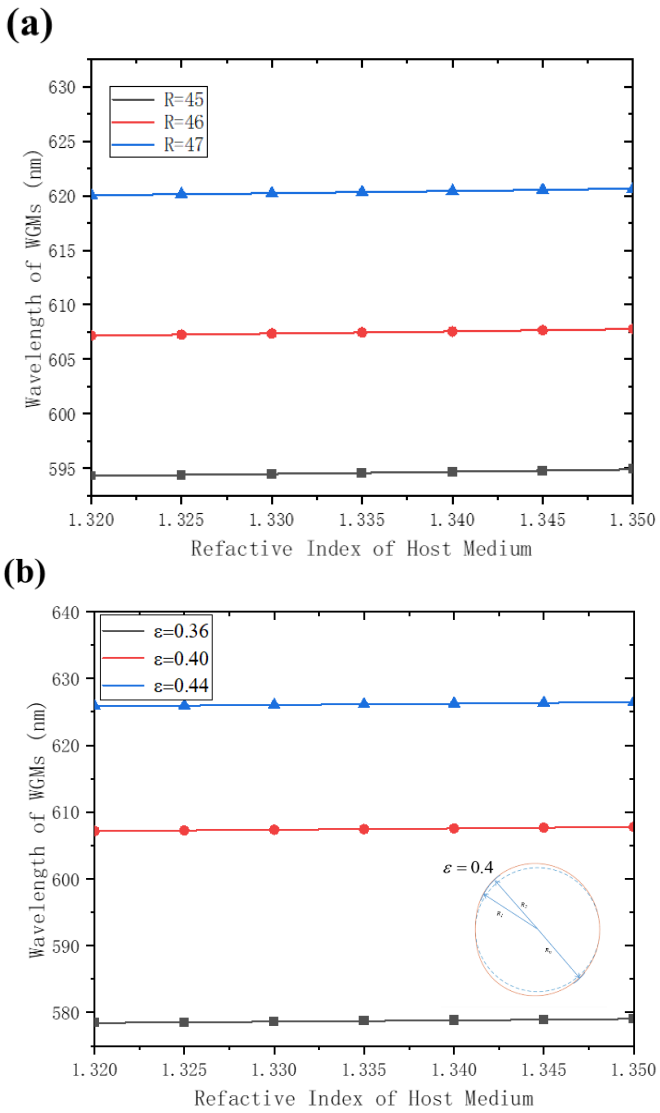

Figure 6 (a) Relationship between wavelengths of WGMs in Limacon-shaped microcavities, the size of microcavity and the refractive index of host medium ($\varepsilon = 0.4$); (b) Relationship between wavelengths of WGMs in Limacon-shaped microcavities, the deformation parameters of microcavities and the refractive index of host medium ($R = 45\mu m$).

In order to investigate the refractive index sensitivity of the Limacon-shaped microcavity, we used circular arcs of different diameters to fit the contour of the deformed microcavity, as shown in illustration of **Fig**. 6 (b). Based on **Fig**. 5 and the equation 3-1 obtained from it, we can calculate the wavelength of the WGM underlying the deformed microcavity. Plotting the obtained results in a graph, we can get **Fig**. 6 (a). At a fixed degree of deformation of the microcavity, the relationship between wavelengths of WGMs in Limacon shaped microcavities, the

size of microcavity and the refractive index of host medium is shown in **Fig**. 6 (b). And when the size of the microcavity is fix, the relationship between wavelengths of WGMs in Limacon shaped microcavities, the deformation parameters of microcavities and the refractive index of host medium is shown as **Fig**. 6 (b).

Based on these results, we can calculate the refractive index sensitivity of the deformed microcavity. For example, the refractive index sensitivity of a deformed microcavity laser is about 20.03nm/RIU when the refractive index of host medium is near 1.333 and a Limacon shaped microcavity with R=45 μm, $\varepsilon = 0.4$.

3.3.2 Sensitivity analysis of elliptical WGM microcavity sensors

The elliptical cavity's contour is defined as

$$\rho = \frac{R \cdot (1 - e^2)}{(1 - e \cdot \cos\theta)} \tag{1.4}$$

where $e \in [0,1]$ represents the eccentricity of the elliptical cavity.

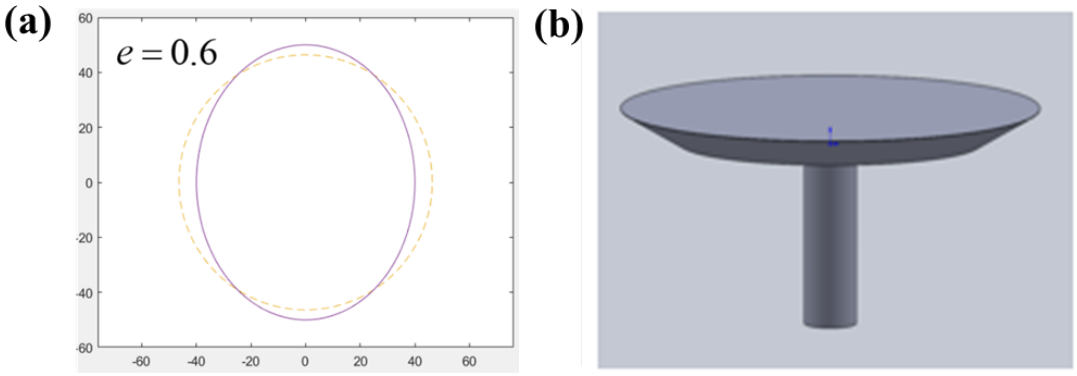

Figure 7 Schematic of (a) an elliptical cavity and (b) the 3D model of elliptical microcavities prepared by using Solidworks.

Figure 7(a) is the schematic picture of an ellipse when the eccentricity is 0.6. Similarly, the ellipse also breaks the perfect rotational symmetry of the cavity. It is because that the contour of the elliptical cavity has larger curvature at some positions and smaller curvature at other positions compared to a circular microcavity. **Fig.** 7(b) shows the 3D model of the suspended

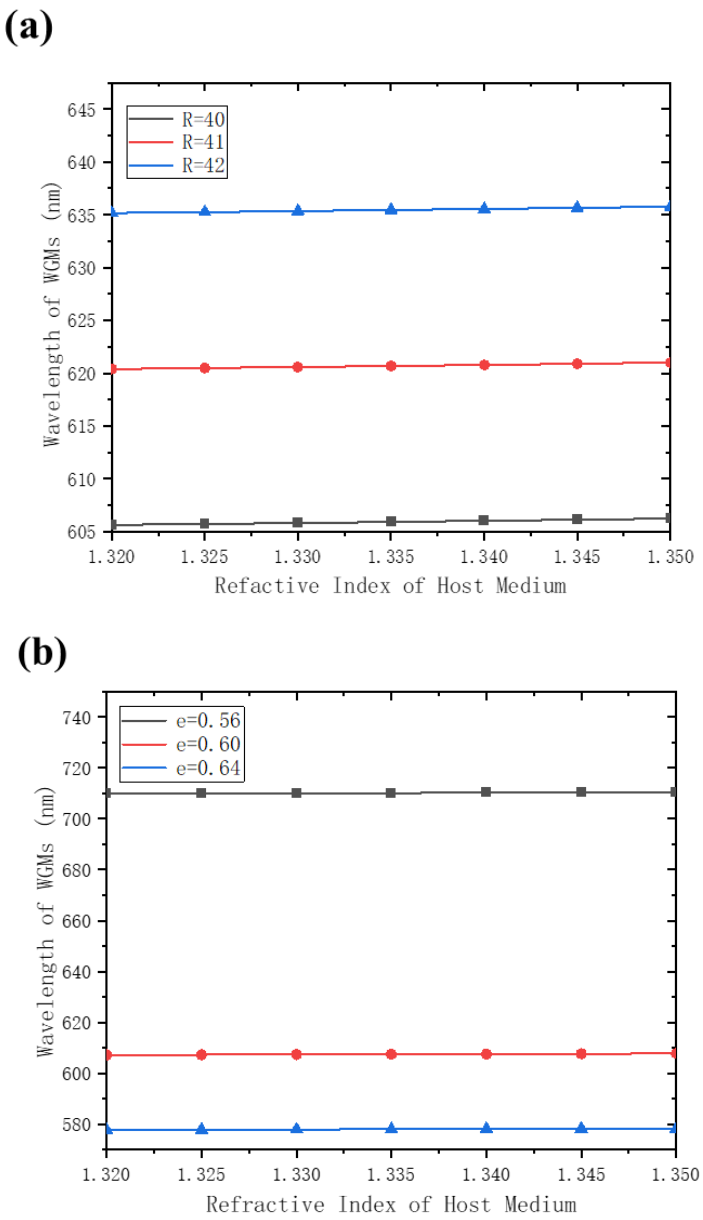

Figure 8 (a) Relationship between wavelengths of WGMs in elliptical microcavities, the size of microcavity and the refractive index of host medium ($e = 0.6$); (b) Relationship between wavelengths of WGMs in elliptical microcavities, the eccentricity of ellipse and the refractive index of host medium ($R = 40\mu m$).

microdisk cavity that we generated using Solidworks based on this shape. Since the radius of deformed cavities is not uniform everywhere compared to circular cavities, we explored the distribution of WGMs in microcavities with different radius.

Similarly, based on the results in **Fig**. 8 and function 3-1, we can calculate that the detection sensitivity of an elliptical microcavity with a radius of 40 μm is 19.88nm/RIU when the refractive index of the external environment is near 1.333.

3.4 Simulation of the directional emission of WGM microlasers with deformed microcavities

The most straightforward design approach to demonstrate the differences between deformed and circular microcavities is ray simulation.

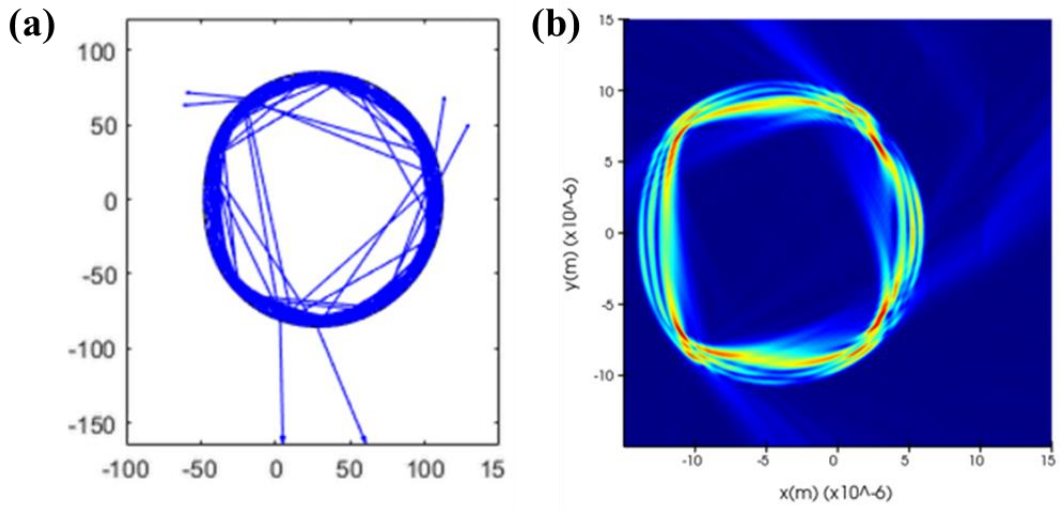

Figure 9 Simulation of the dynamical behavior of light inside deformed microcavities.

As shown in **Fig**. 9, the light ray and wave optic simulations show the dynamical behavior of different shapes of microcavity ray trajectories. In this simulation, we defined the refractive index of the microcavity as 1.57, set the loss of the microcavity as 5% attenuation per millimeter, and set the energy of the incident light as 100. Then we randomly set the incident

optics and analyze the trajectory of the light inside the microcavity by using the vector form of the refraction equation. Due to the good central symmetry, the ray trajectory in a circular microcavity is more regular and the central part of the microcavity is always free of light trajectories. In contrast, due to symmetry breaking, deformed cavities, such as Limacon-shaped and elliptical microcavities, have not only WGM modes whose trajectories cover a larger region of the microcavity but also directional emissions in some directions.

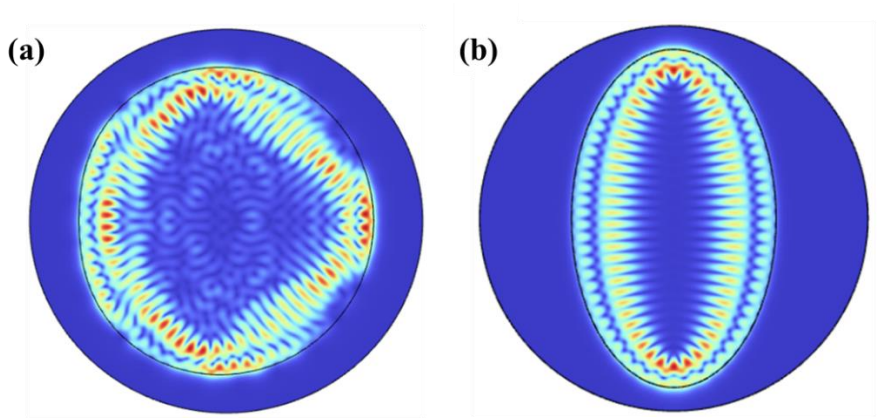

Figure 10. Simulated mode distributions in (a) limacon-shaped and (b) elliptical WGM cavities.

The distribution of the mode field inside the microcavity is another issue worth investigating.

By analyzing the mode field of the microcavity, as Fig 10. shows, we can see that both Limacon-shaped and elliptical WGM microcavities revealed chaotic mode field distributions. These results revealed that the geometrical symmetry of such deformed microcavity has been broken which lead to directional emission. On the other hand, the stable mode distribution of such deformed microcavities indicates that they can still keep a relatively high Q value.

3.5 Summary

In this chapter, we begin with a detailed analysis of the sensitivity of weakly deformed WGM microcavities to the change of external refractive index using the commercial software COMSOL Multiphysics. The results showed that the WGMs of these weakly deformed microcavities are quite sensitive to the change of refractive index in external medium.

We also simulated the optical dynamics inside the weakly deformed WGM microcavity using Matlab and COMSOL Multiphysics. The simulation about the light rays inside the microcavity proved that the deformed microcavity has the ability of directional emission radiation. Simulations on the distribution of WGMs inside the deformed microcavity, on the other hand, demonstrate the effect of symmetry breaking of such deformed microcavities on the distributions of their WGMs, explaining the reason why the WGMs inside the deformed microcavity can achieve directional emission while having a high Q value. In conclusion, through the above series of simulations, we can conclude that the deformed cavity can obtain good directional emission performance while maintaining relatively high sensitivity.

Chapter 4. Fabrication and testing of cavity-deformed WGM microlaser sensors

4.1 Introduction

3D standalone WGM microcavities are typically fabricated by photolithography plus etching and reflow processes. They can also be fabricated by 3D nanofabrication technology, such as two-photon polymerization, and so on. However, although these technologies have the advantage of high resolution, they are typically expensive and low yielding.

In this chapter, we will firstly present our fabrication of the designed WGM microlaser sensors by using optical 3D micro-printing technology. The system uses a DMD chip as the core component and can dynamically project light patterns from the DMD chip onto the SU-8 photoresist layer. The efficiency of microcavity fabrication is greatly improved by the fact that the system enables fast exposure of megapixel images. At the same time, since the entire fabrication process does not require the use of masks, the cost is greatly reduced.

Then, the experimental processes for fabricating the microcavity laser are presented. First, we selected SU-8 photoresist as the photopolymer material for the fabrication of WGM microcavities. To make the fabrication more convenient and reliable, we optimized the formulation of SU-8 photoresist through experiments. To further make a WGM microcavity into a WGM microlaser, we spin-coated a thin layer of Rh6G doped SU-8 on the surface of the microcavity as optical gain medium.

A optical pumping setup is then built for testing of WGM microlasers. Experimental results show that our deformed microcavity also has a high Q value, which can reach the 10^4 level. The microlaser made from this has a very low threshold and the linewidth of the spectral lines

is also very narrow. Meanwhile, the WGM microlasers with deformed microcavities have good directional emission, which is consistent with our design.

4.2 Optical 3D micro-printing technology

Our own-developed optical 3D micro-printing system can rapidly print polymer optical microcavities of various shapes. The key components of our 3D micro-printing system include a digital micromirror device (DMD), a projection system, an XY-axis motorized stage, a vertical motorized stage, and a UV light source (UV lamp: OmniCure S2000, Lumen Dynamics, Canada).

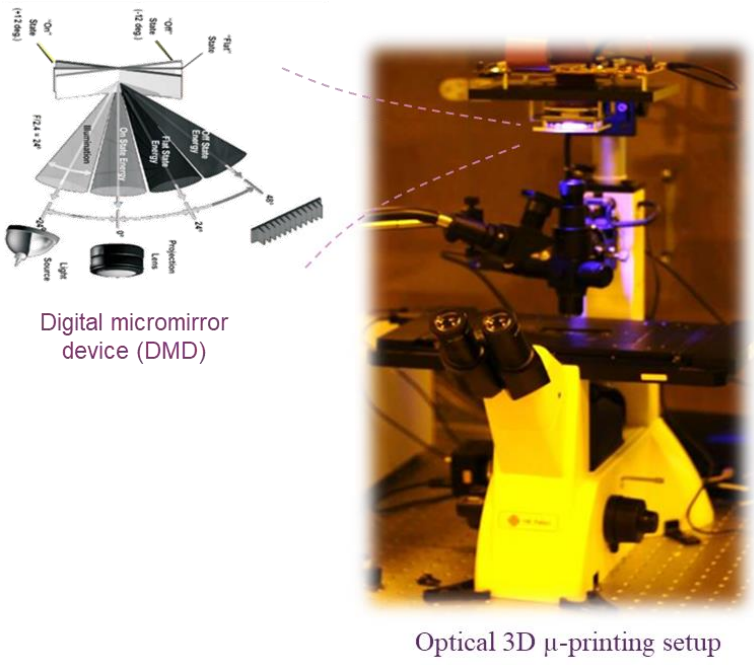

Figure 11 Photo of our optical 3D micro-printing system and the key component, i.e., digital micromirror device (DMD).

Figure 11 shows a photo of the 3D micro-printing system, in which the DMD board was mounted at the top. The main function of the DMD board is to dynamically generate the gray-scale patterns that we designed in advance. When a pixel in the image is white, the micro-reflector at the corresponding position on the DMD will flip 14° in one angle and vice versa.

Thus, using a projection system illuminated with UV light, we can project the pattern on the DMD onto a photoresist prepared by a spin coating process. Arrayed microcavities can be printed by accurately controlling the movement of the XY stage on which the sample was placed.

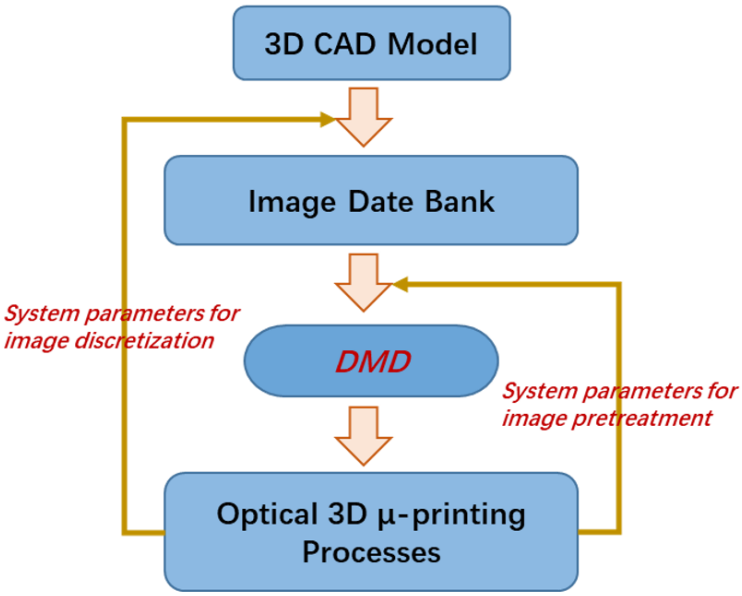

Figure 12 Flowchart of the preparation of image data for 3D micro-printing processes.

The flowchart of the preparation of image data for 3D micro-printing processes is shown in **Fig**. 12. First, patterns of the designed models of the WGM microcavities in BMP format will be uploaded to the DMD board through the software. Afterwards, the patterns on the DMD will be projected onto a glass substrate spin-coated with SU-8 by means of a projection system. To fabricate the 3D structure of microcavities in a thick SU-8 photoresist, different patterns will be dynamically projected to the different positions of the SU-8 photoresist through adjusting vertical (i.e., z) position during exposure process.

4.3 3D micro-printing of WGM microlasers with deformed microcavities

4.3.1 SU-8 photoresist formulation and preparation

SU-8 derives its name from the presence of 8 epoxy groups [68, 69]. It is a negative photoresist with a wide range of applications in micro and nanofabrication. Due to their good optical and mechanical properties, they can be used to fabricate 2D/3D microstructures for a variety of different purposes.

SU-8 resist is a chemically amplified photoresist and the main components are SU-8 monomers, organic solvent, and a photo-acid generator (PAG). SU-8 series photoresists use gamma-butyrolactone or cyclopentanone as the primary solvent. SU-8 was widely used in microelectronics [70-73]. The photoinitiator OPPI in SU-8 photoresist absorbs photons and undergoes a photochemical reaction to produce a strong acid, which initiate an acid catalyst in post-bake and facilitate the cross-linking reaction to occur. The strong acid only present in the exposed position, but not in the unexposed position. The cross-linking reaction grows in a chain, with each epoxy group reacting with other epoxy groups in the same or different molecules to form a dense cross-linked network. This network is insoluble in the developer, while the photoresist in the unexposed areas is dissolved by the developer. Therefore, in our fabrication process, SU-8 solid and OPPI are dissolved in cyclopentanone respectively and then mixed to prepare a photoresist solution that can be spin-coated on glass surface.

To fabricate high-resolution suspended 3D microstructures, we optimized the UV absorption property of the photoresist by changing the formula of the SU-8 solution. First, we prepared two SU-8 solutions, i.e., a 65% solution of SU-8 without UV dye and a 65% solution of SU-8

with UV dye. This dual-layer photoresist is designed to reduce exposure time. It also helps to make thinner suspended microdisks, i.e., the WGM cavity.

Moreover, to make the binding between whole structure and the substrate stronger, we prepared a buffer layer upon glass substrate. In the fabrication, we spin-coated a 15% SU-8 layer onto the glass substrate and exposed it using UV LED for polymerization.

	70% SU-8 Solution	Cyclopentanone	Photoinitiator (OPPI)	UV 234	Inhibitor (TBA)
Layer 2	***x***	*0.046**x***	*0.0175**x***	*0.006**x***	*0.00045**x***
Layer 1	***x***	*0.052**x***	*0.0175**x***	/	*0.00045**x***
Buffer layer	***x***	*3.6495**x***	*0.0175**x***	/	/

Table 4. Relative weights of different constituents in SU-8 solution for different layers.

In our experiments, EPON resin SU-8 was purchased from Momentive Performance Materials. OPPI was purchased from Hampford Research. TINUVIN 234 was purchased from Sigma-Aldrich. Tributylamine (TBA) was purchased from Meryer Chemical Technology.

The relative weights of different constituents in SU-8 solutions for different layers are given in **Table** 4. The weight ratio between SU-8, OPPI and photo-inhibitor (TBA) is 97.5:2.44:0.06. They are typically placed in a glass bottle with magnetic stirring bar for mixing for more than 3 days. It is important in preparing SU-8 solution that we must make sure that the solution is well stirred so that the various components are fully dissolved in the solution. At the same time, the stirring process should not be too fast to avoid the production of air bubbles in the solution. The solution after stirred needs to be filtered to ensure that the solution is free of particles or impurities that are not completely dissolved.

4.3.2 Optical 3D micro-printing processes

The flow chart of optical 3D micro-printing processes is shown in **Figure** 13.

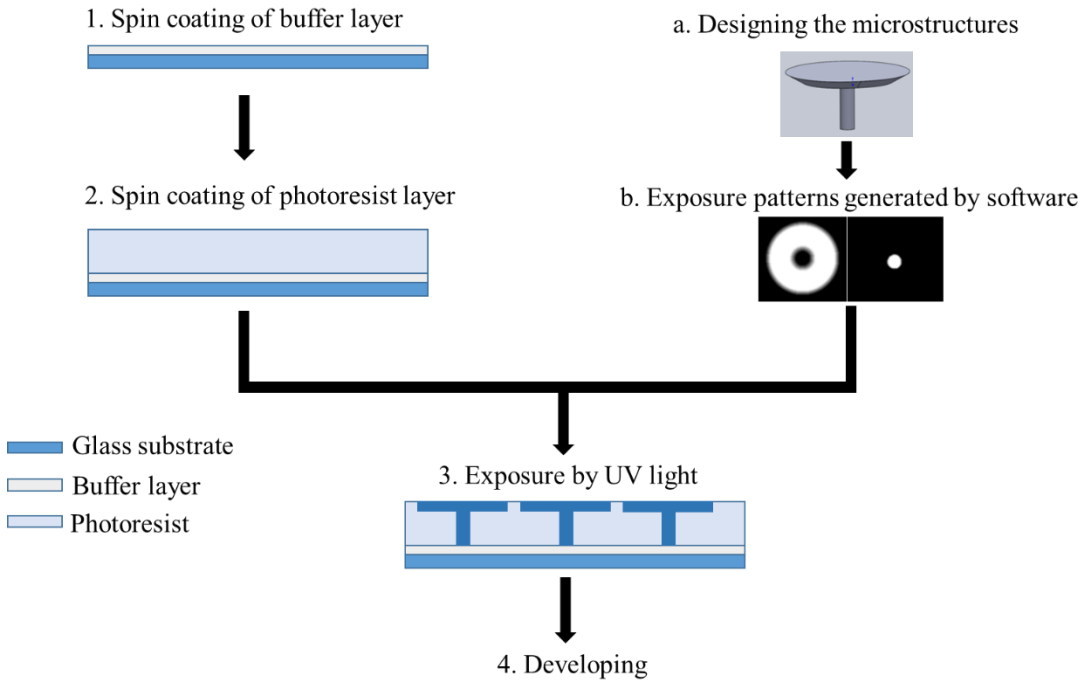

Figure 13 Flow chart of exposure processes.

1) Preparation of glass substrate and buffer layer

The glass substrate was rinsed with IPA and wiped with a dust-free cloth. It was then put into a beaker with acetone for ultrasonic cleaning for 3 to 5 minutes. It was then dried with a high-pressure air gun. It was finally put into a plasma machine for plasma cleaning treatment for more than 60 seconds.

To increase the adhesion between 3D SU-8 microstructure and the glass substrate, we made a thin buffer layer on the glass substrate. Here we used the 15% SU-8 solution prepared earlier and chose the spin-coating parameters as, low speed 500 rpm for 5 seconds and then high speed 1500 rpm for 30 seconds to make the buffer layer thickness around 3 μm.

After spin coating, the glass wafer was placed on a hotplate at 65℃ for 1 minute, followed

by a bake at 95℃ for 5 minutes. The next step is to expose the buffer layer under a UV lamp with a wavelength of 365nm for 15 minutes. This step should ensure that the exposure dose is sufficient. At the end of the exposure, it also needs to be post-baked. After trial experiments, we chose to post-bake the samples at 95 ℃ for 12 minutes.

2) Spin coating and soft-bake processes

The next step is spin-coating of the lower layer of photoresist to make the pillar structure of the WGM microcavities. The process is similar to that of the spin-coating of the buffer layer. For this layer we used SU-8 photoresist without UV234 at a concentration of 65% for spin coating. Previous experiments showed that SU-8 photoresist without the addition of UV234 is easily penetrated by UV light. So, we used SU-8 photoresist without UV234 in the lower photoresist to shorten the exposure time for supporting pillars. Then, the speed and time of spin coating, we used 500 rpm for 10 seconds and 1500 rpm for 50 seconds for this layer. It is then placed on a 65-℃ hot plate and baked for 1 minute, after which it is transferred to a vacuum oven at 70℃ and baked for 60 minutes.

The spin coating process for the upper layer is almost the same as the first layer. The only difference is we used a 65% SU-8 photoresist solution containing UV234. The SU-8 photoresist containing UV234 requires a much larger exposure dose to be penetrated by light. Therefore, we used it as the upper layer to fabricate very thin microdisks. After trial experiments, we have proved that the SU-8 coating can be obtained with a very flat upper surface by setting the oven to 70℃, 0.07MPa, and baking for 60 minutes. With a two-step spin-coating process, we can obtain two layers of SU-8 coatings each of which has a thickness of 30 μm, and thus the total thickness of SU-8 photoresist is about 60 μm.

3) Optical exposure processes

Before exposure, we measured the light power of the UV lamp. We set the lens aperture to

6, set the output of the UV lamp to 100%, and then measure the light power using an optical power meter. Typically, it was about 30 mW. If the measured power is significantly lower than this value indicates that the optical path has shewed or the UV lamp needs to replace the bulb.

First, the prepared glass wafer with SU-8 photoresist was placed in the middle of the XY motorized stage. There are many parameters to be set for exposure process, including dx, dy, dz, UV light power, exposure time, and grayscale levels, etc. Here, dx, dy represents the interval between two exposures. We set a 3×12 matrix, dx set to 0.25 represents the distance between each of the 12 columns. dy represents the distance between each row. When we set dy to 0, we will be able to stack the 3 rows of different dz, in which dz represents the relative z position with respect to the initial vertical position.

Since the structure of the designed WGM microcavity is a 3D suspended structure, we need three layers of exposure positions for one structure, the top layer for projecting the image of the disk, which is the main structure of the WGM microcavity, and the bottom two layers for projecting the image of the supporting pillar. Due to the high absorption and reflection of UV light inside the SU-8 photoresist containing UV234, the photoresist located at the bottom absorbs fewer photons compared to the surface, so we need two or even three layers for the exposure of the bottom pillar, while longer time and higher optical power are needed to ensure that the subsequent can be fully cross-linked.

Based on the absorption curve of SU-8 photoresist for UV light and the structure we expect to obtain, we exposed the bottom of the SU-8 photoresist, especially the part connected with the glass substrate, sufficiently to make the OPPI absorb sufficient light to produce hydrogen ions for promoting the cross-linking of SU-8 and thereby achieve a stable and solid structure. As for the WGM microcavity at the top, in order to suppress unnecessary stray modes as much as possible, we have to make sure the edge thin and smooth enough to get the highest possible Q value. Therefore, we chose a relatively low UV power when exposing the top structure and

change the UV absorption curve of SU-8 using UV234 so as to make the thickness of the microdisk exposure tailorable in the range of within a reasonable range.

Exposure time and light power together determine effective exposure dose in SU-8 photoresist for photopolymerization. We use the gray scale map of 0 ~ 255 levels from pure black to pure white. Correspondingly, the system supports the maximum gray scale levels of ~255 layers, that is, the gray scale values will be mapped into 255 different exposure time. For a BMP image, the whiter the region has longer exposure time, while the black will not be exposed. So, we can use the gray scale value to tailor the edge of the microcavity to achieve a wedge structure.

In experiments, the intensity of UV light was set at 30% to 40% of the maximum power (i.e., 30 mW). Too low exposure dose will result in a result that are prone to be micro-deformed, which in turn leads to less fineness. On the other hand, too high dose will make the microdisk too thick and the shape of the edge contours difficult to be tailored. The above shows a parameter file using different light source power exposure, because the speed of our control software to update images to the DMD is limited. To alleviate this limitation, a lower UV light intensity was used in the exposure, which can extend the exposure time appropriately. For instance, we typically use 10% of the light power to expose the microdisk to precisely tailor the shape of its edge.

The grayscale image is the data file for controlling optical projection which thus determine the shape of final printed structure. During the design of image data, we need consider not only the physical structure of the designed WGM microcavities, but also some effects resulting from printing processes. For example, the middle of the pattern for the suspended microdisks are designed to include a hole with grayscale transition. The purpose of such a hole is avoid overexposure in middle of the structure as the photoresist of this part has been exposed during the exposure of supporting pillar. A grayscale region is applied to compensate the scattering

induced unwanted exposure of the region around the pillar. On the other hand, a grayscale transition region is also adopted to the edge of the pattern. The purpose of this grayscale transition region is to tailor the edge of microcavity to form a wedge for the designed WGM microcavities.

The typical size of grayscale images were 420 × 420 pixels, which were generated by using Matlab and then saved to BMP images, as shown in **Fig** 14. The real size of each pixel corresponds to about 1.1 μm × 1.1 μm in our optical 3D microprinting system.

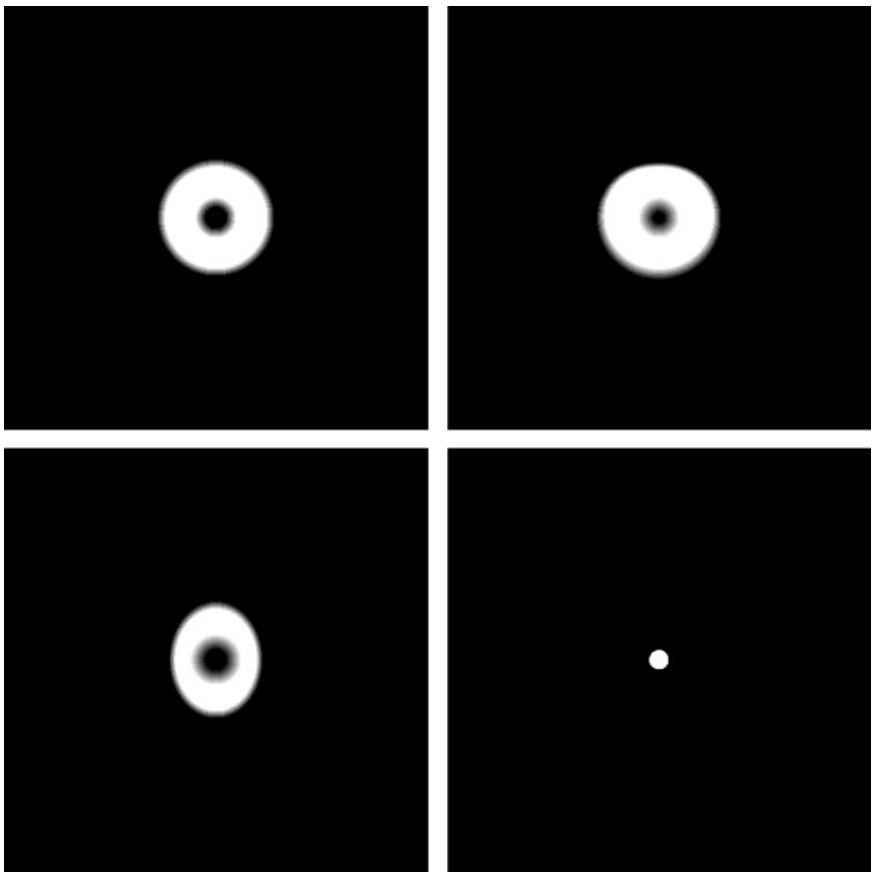

Figure 14. Grayscale images used in the 3D microprinting of our designed WGM microcavities and supporting pillars.

4) Post-Bake, development and hard-bake processes

Post-baking is also a very critical step. Proper settings of baking time and temperature as

well as ramp-up and ramp-down curves will make the structure fully cross-linked and thus more stable. We baked the first sample on an electric plate at 65℃ for 30 minutes after the exposure was completed.

According to traditional lithography processes, SU-8 photoresist needs post-baked at 65℃ and 95 ℃, sequentially. But according to scanning electron microscopic images, we noted that 95-℃ post-baking will cause a severe shrinking on the edge of the printed 3D structures. In order to solve this problem, according to the experience of the reference [74], we removed the post-baking at 95 ℃ and extended the post-baking at 65 ℃ to 30 minutes. Experimental results showed that such a change can make the edge of the microdisk structure maintain a height the same with the central part and thus efficiently solve the edge sagging problem.

After post-baking and cooling, the sample was fully immersed into a developing solution. We set the development time to 15 minutes based on trial experiments, and then IPA is used to rinse off residual SU8, developing solution, and dirt and particles that were fallen on the surface of the sample. If there is still residual SU-8 found after washing, the development process can be conducted once more time.

Hard baking is the final step, which can increase the hardness and stability of the structure and makes the surface smoother. After trying of a variety of hard baking conditions, such as hard baking temperature as well as heating and cooling curves, we finally chose 155 ℃ as the peak temperature, which has the greatest impact on the result. After maintaining the peak temperature for 20 minutes, the sample was cooled down naturally to room temperature.

The parameters of each step in the whole WGM microcavity fabrication process are shown in **Table** 5.

		Temperature (°C)	Rotation (rmp)	Duration(s)
Buffer layer (15% Su-8 Solution)	Spin coating		500rmp	5
			1500rmp	30
	Pre-bake	65		60
		95		300
	UV exposure			900
	Post-bake	95		720
Buffer layer (65% Su-8 Solution, repeat two times)	Spin coating		500rmp	10
			1500rmp	50
	Pre-bake	65		60
		65 (vacuum oven, 0.07MPa)		3600
	Post-bake	65		1800
Development				900
Hard-bake		155		120

Table 5. Parameters for the fabrication of WGM microcavities.

5) Spin-coating of the active layer for WGM microlasers

After preparation of high Q microcavities, Rhodamine 6G (Rh6G) doped SU-8 was then spin-coated on the surface of the microcavity for the preparation of WGM microlasers. Rh6G is a fluorescent rhodamine group dye with highly quantum efficiency. It is widely used in biotechnology such as fluorescence microscopy, flow cytometry, fluorescence correlation spectroscopy and enzyme-linked immunosorbent assay (ELISA).

The absorption and fluorescence spectral lines of Rh6G are shown in Fig. 15. Based on the absorption spectral line, we can tell that Rh6G can have a strong absorption around 532 nm and its emission band is around 540 nm to 620 nm. Therefore, we choose to use a pulsed laser with a central wavelength of 532 nm as the optical pumping laser source.

To obtain the desired micro-laser based on the WGM microcavity, we needed to spin-coat a thin layer of Rh6G on the surface of the structure as a gain medium for future testing of its

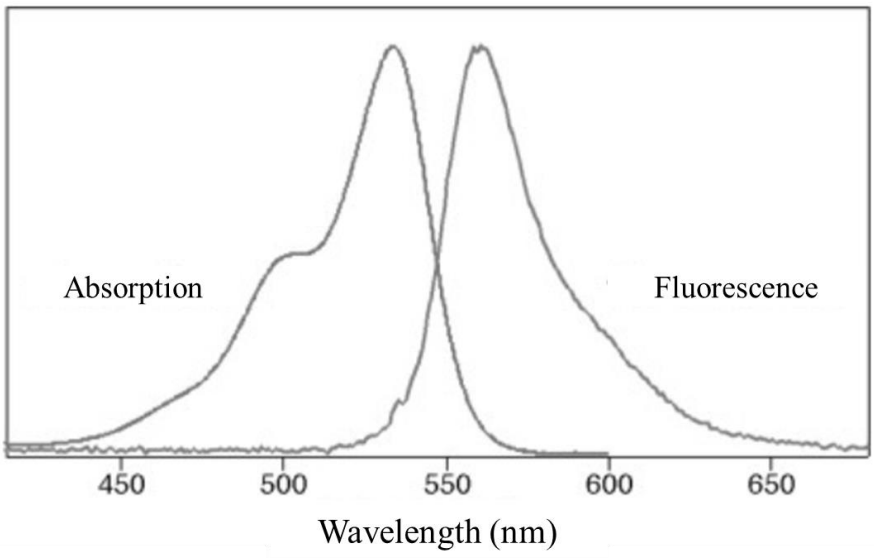

Figure 15 Absorption and fluorescence spectra of rhodamine 6G [75].

laser spectrum and application as a biosensor. Rh6G is first dissolved in ethanol at a concentration of 20 μmol/mL and then mixed with a 15% solution of SU-8 dissolved in cyclopentanone to make sure the concentration of Rh6G is 3μmol/g. We first must treat the microcavity surface using plasma, setting a relatively low voltage and a time of 60 seconds. The mixture of Rh6G and SU-8 is then spin-coated onto the microcavities' surface using 1500 rpm to 2000 rpm held for 30 seconds, followed by soft baking at 65 °C for 15 minutes to remove the solvent.

4.4. Fabrication results of WGM microcavities

To test whether the shape and structure of the printed microcavities coincide well with our designs, we used a field-emission scanning electron microscope (Tescan MAIA3) to take images and check the surface quality of the printed microcavities.

The SEM images of the printed WGM microcavities are shown in **Fig**. 16. The flatness of its upper surface has reached a quite desirable level, as shown in **Fig**. 16 (a) and (b), which indicates that our printed microcavities have a high Q value. From **Fig**. 16 (c) and (d), we can see that the shape of the microcavity matches with our design very well.

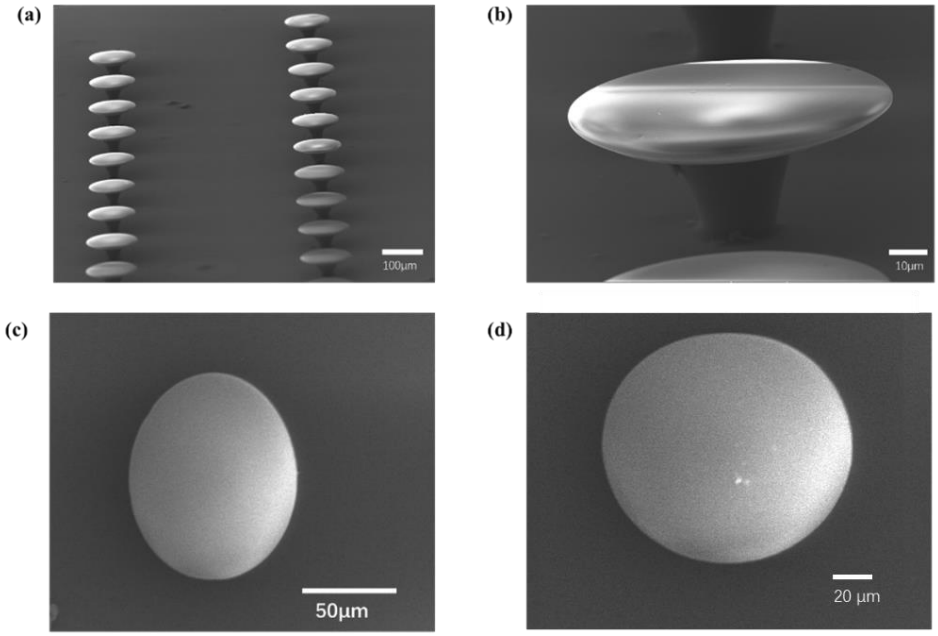

Figure 16. (a) SEM images of the printed WGM microcavity array. (b) Side view of a single microcavity. (c) Top view of an elliptical WGM microcavity. (d) Top view of a Limacon-shaped WGM microcavity.

4.5 Testing of WGM microlasers with deformed microcavities

4.5.1 Pumping test setup for WGM microlasers

The most common scheme for utilizing laser pumping microcavity lasers is vertical pumping from top to bottom. In order to realize this, we have constructed a laser-pumping microcavity set up independently in our laboratory.

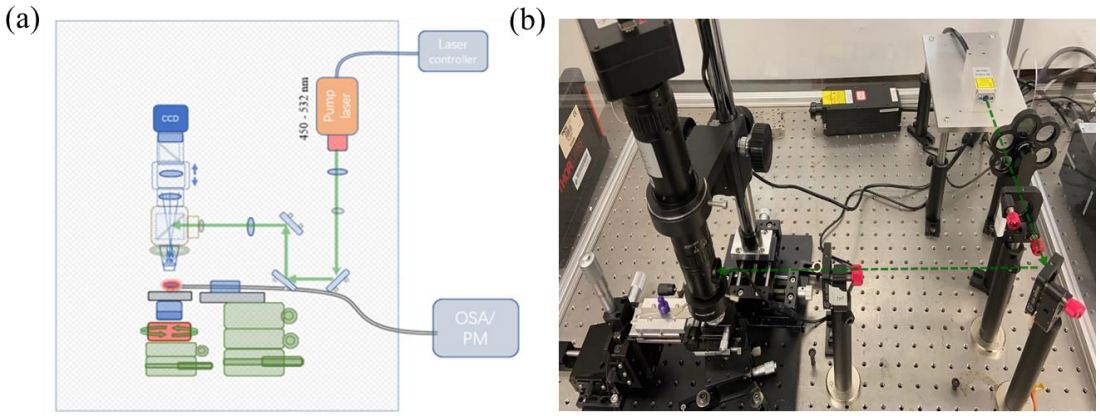

Figure 17 (a) Schematic diagram of the pumping test setup and (b) Photo of the pumping test setup.

As shown in **Fig**. 17(a), the optical path of the whole pumping system is divided into three main parts. The first optical path consisting of a light source, a collimating lens with a focal length of 30 mm, a lens with a focal length of 200 mm, and a 10× objective lens that compresses the spot to a diameter of about 150μm is used to accurately pump individual microcavities. The other optical path, consisting of the same objective lens, as well as an imaging system, a CCD, is used to align the sample with the spot, as well as the sample with the optical fiber used to collect the emission light. Between the CCD and the objective lens, a notch filter with a cutoff wavelength of 532 nm was used to block the pumping light when taking the images of WGM patterns. These two beams are combined by a 70:30 beam splitter, thus sharing the same objective lens. Here, the beam splitter is purposely placed so that more energy on the pump path hits the sample. The last optical path consists of a collection fiber connected to an ultra-high precision spectrometer.

The light source used in the pumping setup is an MPL-T laser purchased from Changchun New Industry Optoelectronics Tech. Co., Ltd., which has a single-pulse energy of about 1μJ, a repetition frequency of 10 Hz, and a single-pulse duration of about 5 ns. The shape and dimensions are shown in **Fig**. 17(a) and (b). The lens for the imaging optical path is a variable magnification commercial lens purchased from Mvotem Optics. This lens allows for 0.6 to 4x zoom. The spectrometer used for the whole setup is a spectrometer with very high sensitivity and resolution to meet the demand for spectral resolution. The spectrometer was purchased from Hong Kong Optime Technology Co., Ltd. And the item code of the spectrometer is HF-9332 and brand is LightMachinery. Its spectral width is from 450nm-700nm, and its theoretical resolution accuracy is down to 25 pm.

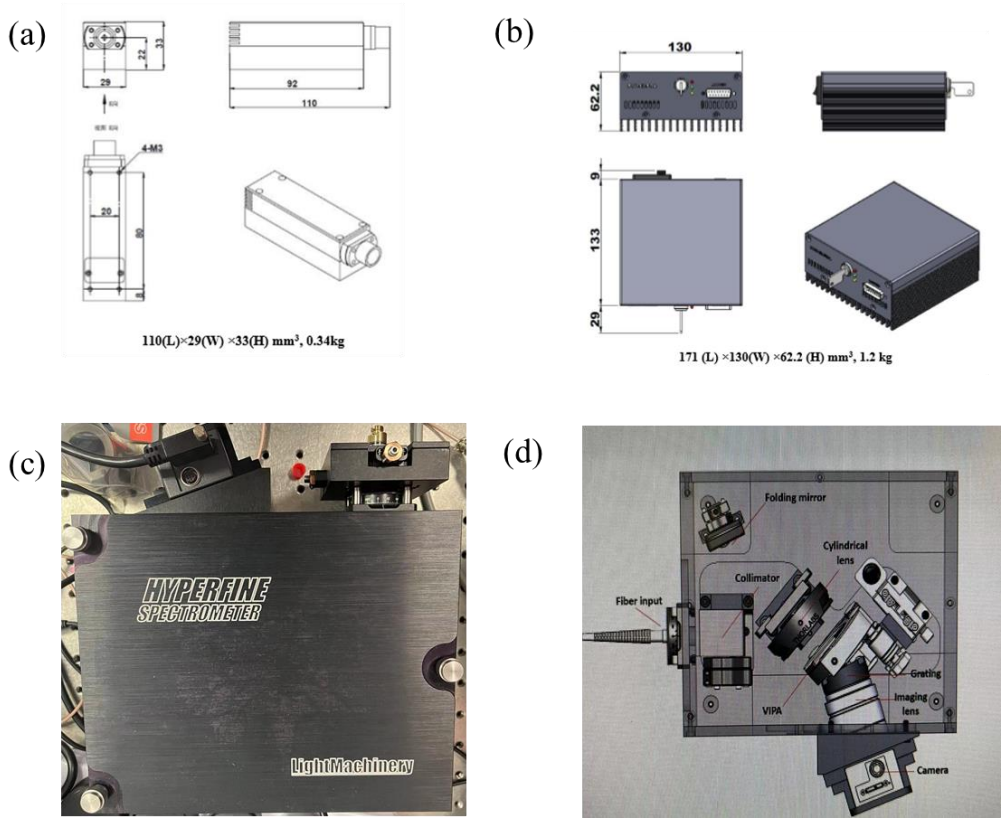

Figure 18. Key components of the pumping test setup. (a, b) Pump laser head and its power supply; (c, d) Photo and the inner structure of a high-resolution spectrometer for pumping test experiments.

The sample stage is a four-degree-of-freedom platform consisting of a three-axis displacement stage and a rotary stage. In experiment, the Z-axis is used to adjust the distance between the sample and the objective lens for focusing. The XY-axis is used to align the microcavity and the pumping spot, and the rotating stage can be used to adjust the angle of the microcavity. At the same time, the platform on which the collection fibers are placed consists of a three-axis displacement stage and a two-degree-of-freedom dovetail. The platform can be adjusted not only for the spatial position of the fiber, but also for the angle of inclination.

4.5.2 Pumping test results of 3D micro-printed WGM microlasers

The first step in the pumping experiment is to accomplish focusing under the illumination of a ring illuminator.

Next, the pump laser is turned on and the pumped spot appears on the screen. Then move the XY axis of the sample stage to align the microcavity with the pump spot. Finally, the fiber optic holder is adjusted until the signal appears on the spectrometer.

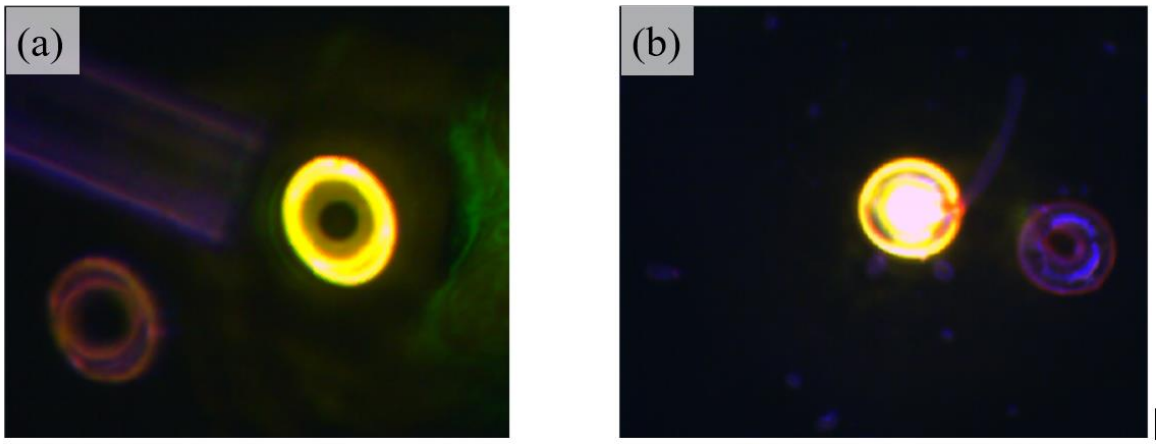

Figure 19 Photos of the WGM microcavity lasers under laser pumping. (a) WGM microlaser with elliptical cavity; (b) WGM microlaser with Limacon-shaped microcavity.

After the adjustment is completed, the effect obtained from the top CCD is shown in Figure 19. The image shows a restricted WG pattern near the edge of the microcavity laser under the excitation of a laser with a center wavelength of 532 nm.

Pumping test results of WGM microlasers with circular microcavity are shown in **Fig**. 20. In the experiment, an attenuator hand wheel with different attenuating plates were used to adjust the power of pumping laser to obtain different pump powers to acquire the laser threshold. The radii of the circular microlaser we used here is 50μm, and the perimeter of the microcavity is 314μm. We measured three samples for each experiment to ensure reproducible results. **Figure** 20(a) illustrates the relationship between the output power and pump power of the microcavity

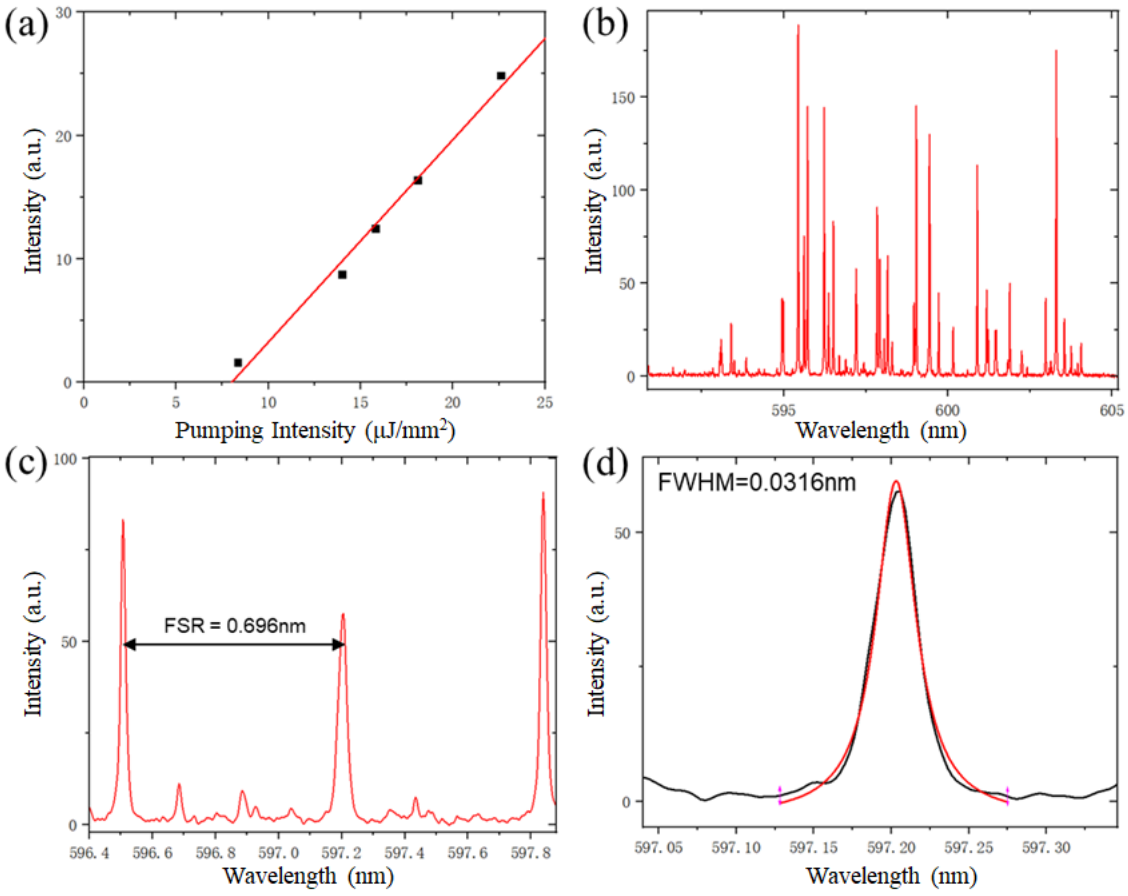

Figure 20 (a) Measured emission power versus pump power of a circular microcavity WGM laser and its linear fit; (b) Emission spectrum of the WGM microlaser; (c) Free-space spectral range (FSR) of the emission spectrum; (d) Lorentzian fit of the WGM centered at 597.21 nm.

laser. The results show that the threshold of the circular laser is about 8.53μJ/mm^2. **Fig**. 20(b) shows the excitation spectral lines of a circular microcavity, which can be seen to have medically spurious modes due to the higher order modes that are unavoidably generated in the microcavity. **Fig**. 20(c) is an enlarged view of the spectral lines and it can be seen that the FSR of the spectrum is 0.696nm. According to equation (1.3), the theoretical value of FSR of our microlaser is $\Delta\lambda_{FSR} = 0.6^2 / (2 \times \pi \times 55 \times 1.57) \approx 0.66nm$ .Therefore, the result of our experiment is in good agreement with the theory. **Figure** 20(d) illustrates a single peak centered at 586.23nm in the spectrum that has a half-height full width (FWHM) as narrow as 0.0316nm

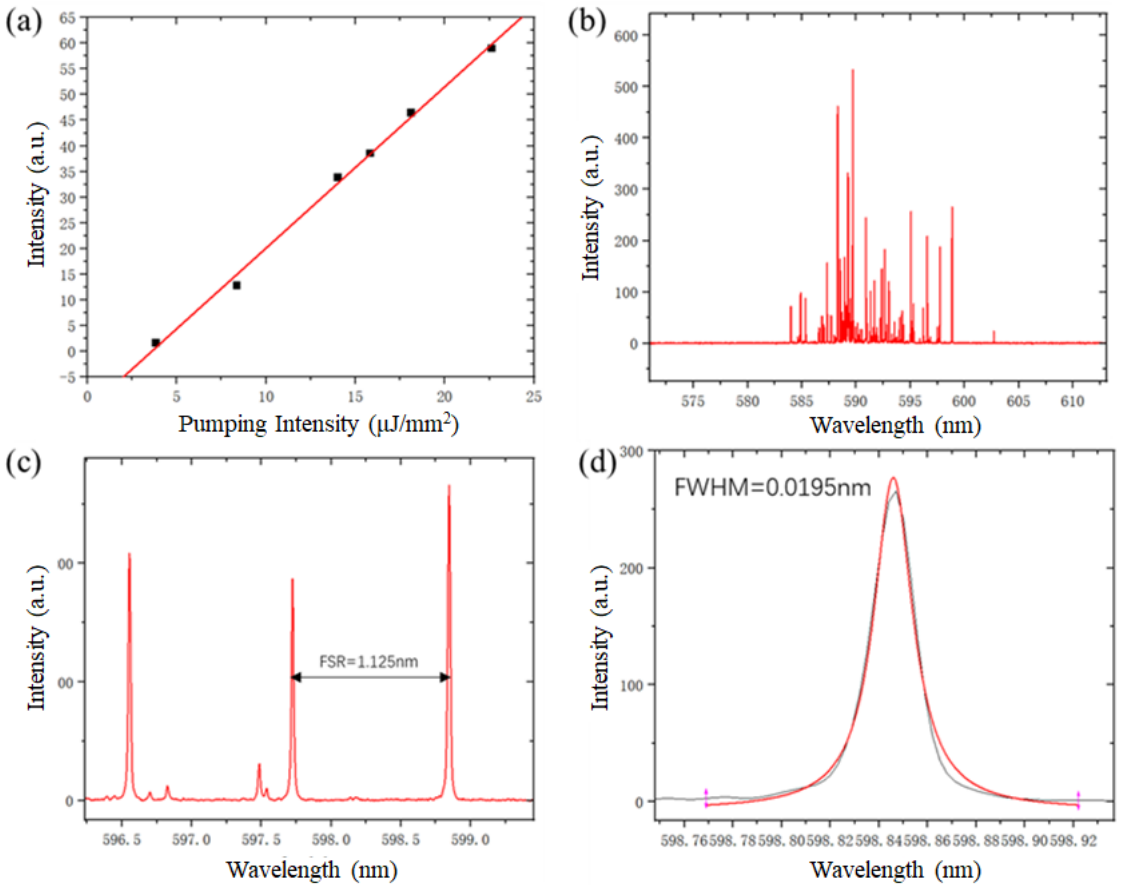

Figure 21. (a) Measured emission power versus pumping power of a Limacon-shaped microcavity laser and its linear fit; (b) Emission spectrum of the WGM microlaser; (c) Free-space spectral range (FSR) of the emission spectrum; (d) Lorentzian fit of the WGM centered at 598.85nm.

(31.6pm). According to equation 1-2, this means that the Q value of our circular microcavity is around 1.86×10^4.

Figure 21 shows the pumping results of limacon-shaped microlaser. **Fig.** 21(a) illustrates the relationship between the output power and pump power of the microcavity laser. The radii of the Limacon-shaped microlaser we used here is 50μm, the deformation coefficient is 0.4 and the perimeter of the microcavity is 314μm. We measured three samples for each experiment to ensure reproducible results. The results show that the threshold of the limacon-shaped microlaser is about 8.53μJ/mm^2. **Fig**. 21(b) shows the excitation spectral lines of a circular microcavity, which can be seen to have medically spurious modes due to the higher order modes that are unavoidably generated in the microcavity. **Fig**. 21(c) is an enlarged view of the spectral lines and it can be seen that the FSR of the spectrum is 1.125nm. Theoretically, combining with equation (1.3), the theoretical value of the FSR between modes is about 0.7 nm if the contour perimeter of the Limacon-type microcavity is calculated as the paths of the WGMs. However, according to Fig. 10(a), the WGMs in the Limacon-type microcavity do not distribute along the microcavity contour, and the paths of the WGMs should be much smaller than the microcavity perimeter. Therefore, the FSR in the laser spectrum here should also be larger than 0.7nm. **Figure** 21(d) illustrates a single peak centered at 598.85nm in the spectrum that has a half-height full width (FWHM) as narrow as 0.0195nm (19.5pm). According to equation 1-2, this means that the Q value of our Limacon-shaped microcavity is around 3.07×10^4.

Figure 22 shows the pumping results of elliptical WGM microlaser. The semi-major axis of the elliptical microlaser we used here is 50μm, and the eccentricity of the elliptical microcavity is 0.6. We measured three samples for each experiment to ensure reproducible results. Figure 22(a) illustrates the relationship between the output power and pump power of the microcavity laser. The results show that the threshold of the circular laser is about 4.87

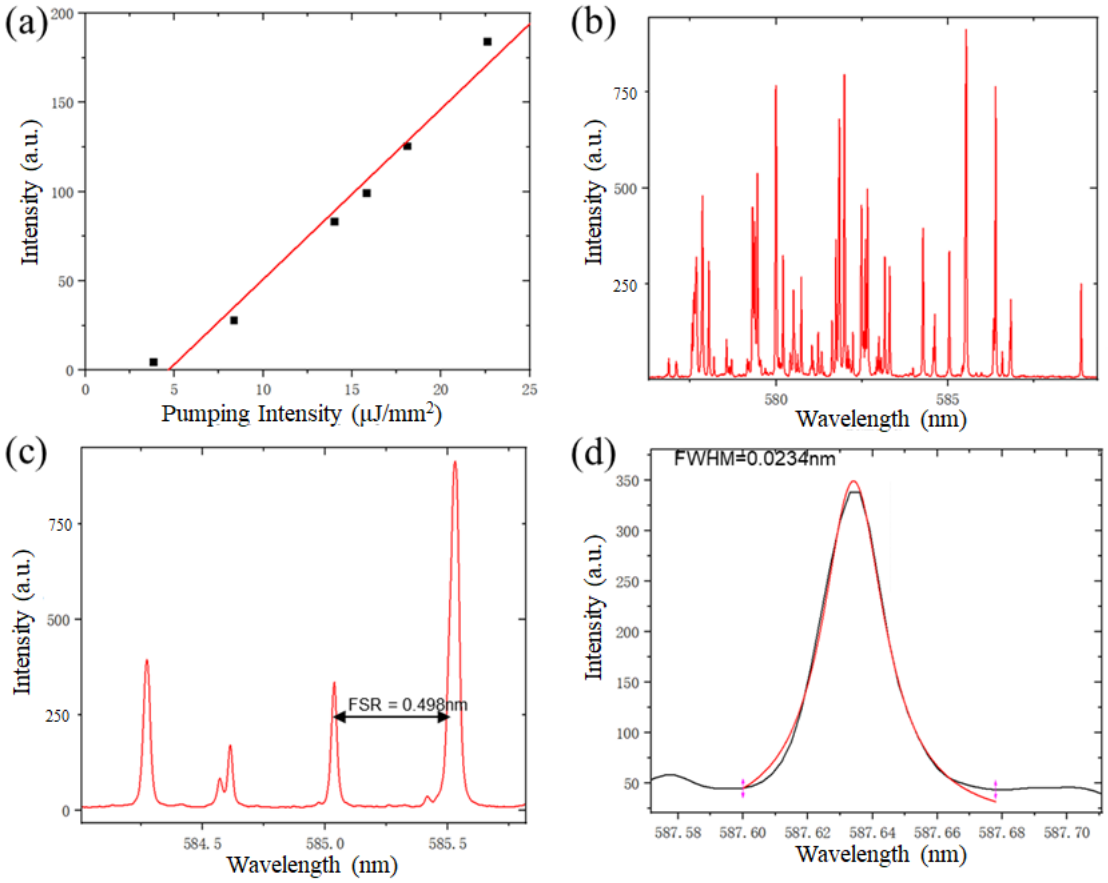

Figure 22 (a) Measured emission power versus pumping power of an elliptical microcavity WGM laser and its linear fit; (b) Emission spectrum of the elliptical microcavity laser; (c) Free-space spectral range (FSR) of the WGM microlaser emission spectrum; (d) Lorentzian fit of the WGM centered at 587.64 nm.

μJ/mm^2. Fig. 22(b) shows the excitation spectral lines of a circular microcavity, which can be seen to have medically spurious modes due to the higher order modes that are unavoidably generated in the microcavity. Fig. 22(c) is an enlarged view of the spectral lines and it can be seen that the FSR of the spectrum is 0.498nm. Similarly, according to equation (1.3), here, the perimeter of the elliptical cavity is about 459.58 μm. According to Fig. 10(b), the WGMs in the elliptical microcavity are essentially distributed along the contour, and thus the paths of the WGMs here are essentially the same as those at the edges of the elliptical microcavity. Therefore, the theoretical value of FSR here is 0.5 nm. Figure 22(d) illustrates a single peak in the spectrum that has a full width at half maximum (FWHM) as narrow as 0.0234 nm (23.4

pm). According to equation 1-2, this means that the Q value of our elliptical microcavity is around 2.51×10^4.

Taken together, all three types of microlasers made of different kinds of microcavities are capable of generating laser light with a relatively low threshold. All three lasers operate in the laser wavelength range of about 580 - 600 nm. So, all the mode wavelengths of the microcavity laser are within the emission range of Rh6G.

Fitting the measured spectrum with a Lorentzian curve, we can obtain the FWHM value of the WGM mode, from which the Q value of the microcavity can be estimated to be around 10^4. Indeed, the FWHM values of all fabricated WGM microcavity lasers are in the order of tens of picometers, which reflects the high quality of our microcavities. The smallest FWHM value is for a circular microcavity laser at 20 picometers and the highest is for an elliptical laser at about 24.9 picometers. From circular microcavity lasers to Limacon shaped microcavity lasers to elliptical microcavity lasers. The FWHM values of the laser modes gradually become larger, reflecting a slight decrease in Q value due to symmetry breaking.

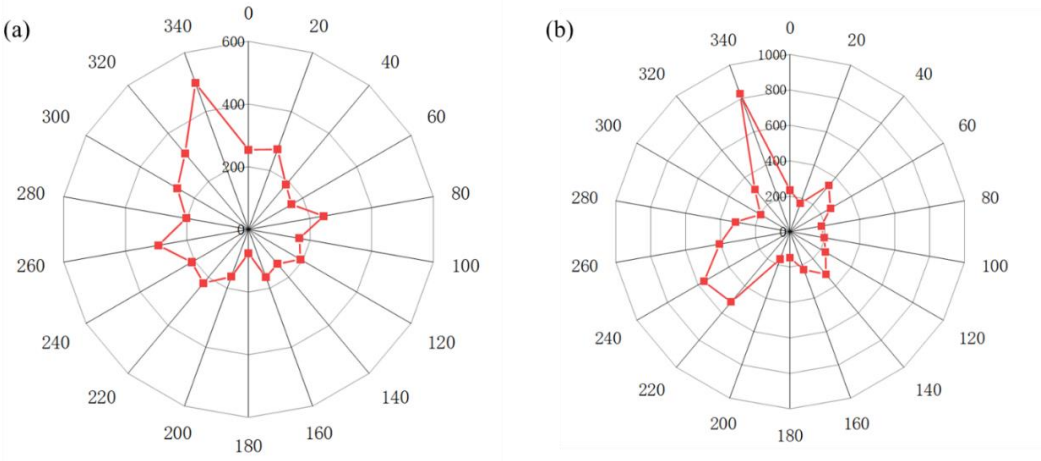

Figure 23. Measured directional emission patterns of (a) Limacon-shaped WGM microcavity lasers and (b) elliptical WGM microcavity laser.

The directionality of the emission from the two fabricated cavity-deformed WGM microlasers has also been measured. A rotation stage is used to rotate the sample and record their emitted power of different directions. The results of the experiment are shown in Figure 23. From **Fig**. 23(a), the Limacon-shaped microcavity laser emits mainly in one direction unidirectionally, which is about 340° in our experiment. Elliptical microcavity lasers, on the other hand, emit unidirectionally in four symmetrical directions, as shown in **Fig**. 23(b). Although the entire far-field emission pattern is not perfectly aligned due to the lack of stability of the measurements, directional emission in the four symmetrical directions of 40°, 140°, 220° and 340° are still clearly visible.

The results of our experiments demonstrate that both of the two cavity-deformed WGM microlasers we fabricated have clear directional emission performance. Meanwhile, the far-field emission pattern is also in good agreement with the theory.

4.6 Summary

In this chapter, we describe in detail the fabrication and testing of cavity-deformed WGM microlaser sensors.

First, we designed an SU-8-based photoresist formulation in-house to facilitate the subsequent fabrication process of different kinds of microcavities with high Q value. After that, utilized a self- constructed digital 3D UV exposure system, we realized the rapid 3D μ-printing fabricating process of different kinds of high-Q microcavities. Afterwards, utilizing Rh6G as the fluorescent dye, we prepared the high-Q deformed microcavities into microlasers with ideal performance.

Experimentally, we have demonstrated that the micro-laser we obtained has an extremely low pumping threshold, which will be beneficial for subsequent bio-detection experiments. At the

same time, thanks to the high Q-value of the microcavities, the peaks in the laser spectrum also have an extremely high degree of fineness, which is a guarantee of high detection limits in subsequent detection experiments. If one wants to further increase the Q value, a material with lower optical loss, such as silica, can be used to print WGM microcavities. Meanwhile, while ensuring the aforementioned laser qualities, our experiments demonstrate that the deformed microcavity-based lasers also have good directional emission performance, which will help to reduce the complexity of collecting laser signals.

Chapter 5. Directly printed high-Q directional-emission WGM microlaser biosensors for label-free biodetection

5.1 Introduction

Highly sensitive detection of biomarker molecules is important in the early diagnosis of diseases. Our deformed-microcavity based lasers can play an important role in this field. Optical microcavities could enhance the interaction between light and matter by confining light to an extremely small space. In our experiments, antibodies to human IgG were modified on the surface of a microcavity laser. When the antigen-antibody binding reactions occur on the surface of the microcavity, the wavelengths of the WGMs in the microcavity will shift. This enables the specific detection of biomarker molecules in serum in an ultra-low concentration.

In order to carry out the test of sensing sensitivity as well as the detection of biological proteins, we actualized the device as shown in **Figure** 24. A glass wafer with microcavities is placed face up as a substrate. Another glass affixed with two coverslips, as shown in Fig. 24(b), will be back-snapped onto the glass substrate. In this way, between the upper and lower glass, a chamber is formed for the liquid to inlet and outlet.

When conducting the experiment, the microcavity and fiber were first adjusted for height and position to make sure that the laser signal could be received from the spectrometer. The liquid to be tested was injected into the chamber between the upper and lower glass wafers using a pipette gun, approximately 15 μL at a time. When removing the liquid, we use filter paper to suck the liquid out of the chamber from the side.

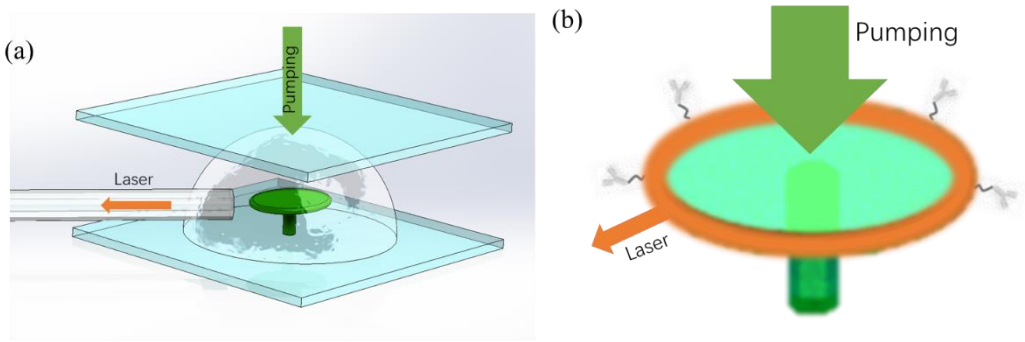

Figure 24. Schematics of (a) the WGM microlaser sensor and (b) the sensing principle for label-free biodetection.

During the experiment, we first tested the stability of the sensor. After that, we investigated the refractive index sensitivity of the sensor. To make sure the whole sensor can work properly. After completing the modification, we tested the ability of the sensor to detect human IgG. The experimental results showed that our sensor could detect human IgG molecules in solution at concentrations down to the ag/mL order of magnitude.

The experiments described in this chapter demonstrate the extremely low detection limit of the deformation microlaser-based biosensor we prepared. At the same time, it is demonstrated that this sensor has high stability. This provides a direction for the future development of portable biosensors with low detection limits.

5.2 Bulk sensitivity tests

In order to examine the refractive index sensitivity of the sensor, we utilized glucose and deionized water prepared into buffer solutions of different concentrations.

According to reference [76], the refractive index of a glucose solution changes with concentration. The relationship satisfies the following equation

$$n_{g/l} = 0.00011889C + 1.33230545 \tag{5.1}$$

where C represents the concentration of the glucose and $n_{g/l}$ represents the average refractive index of the resolution.

Before we started testing the sensitivity, we tested the stability of the sensor, which is the basis for ensuring that it is capable of extremely high sensitivity detection. In our experiments, we filled the sensor with PBS solution and then tested it every 600s and recorded the position of the peaks.

The experimentally obtained spectrum is shown in **Fig**. 25(a). The position of the peaks in relation to time is shown in **Fig**. 25(b). The displacement of the peaks of the signal of the sensor is only about 9.53pm in a time of 2400 s, which proves that the sensor has a high stability.

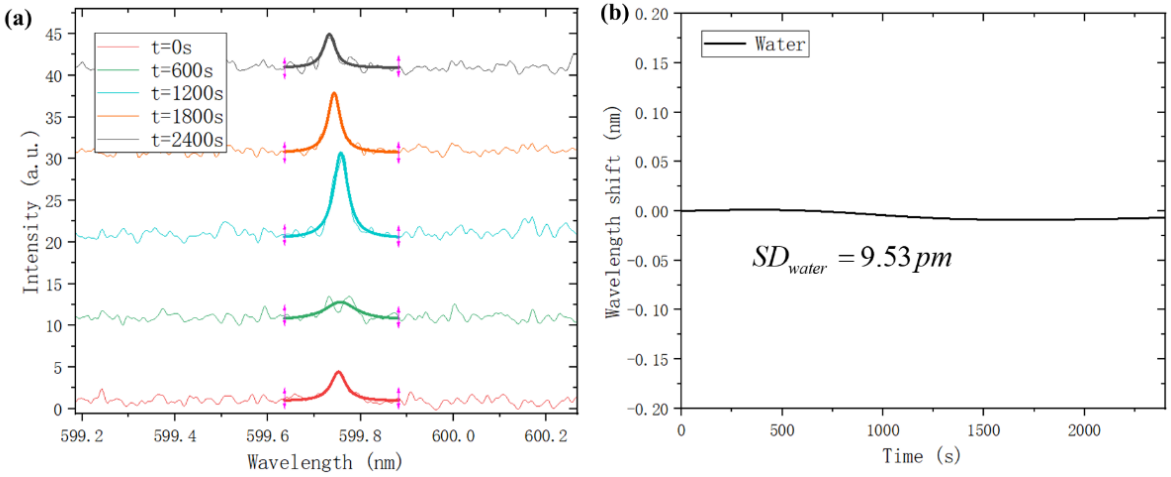

Figure 25 Stability testing results of the fabricated WGM microlaser sensor.

After some pre-experiments, we set the final concentration gradient of glucose solution to 1mg/mL, 2mg/ml, 3mg/mL, 4mg/mL, and 10mg/m. According to Eq.(5.1), the refractive index of each of the five solutions is calculated as 1.33242434, 1.33254323, 1.33266212, 1.33278101 and 1.33349435.

For circular microcavity based microlaser, the experimentally measured data are shown in **Figure** 26(a), and all five spectral lines are plotted onto the same graph. A regular shift of the laser peaks near 601.4 nm occurred. As shown in the figure, after Lorentzian fitting, the center

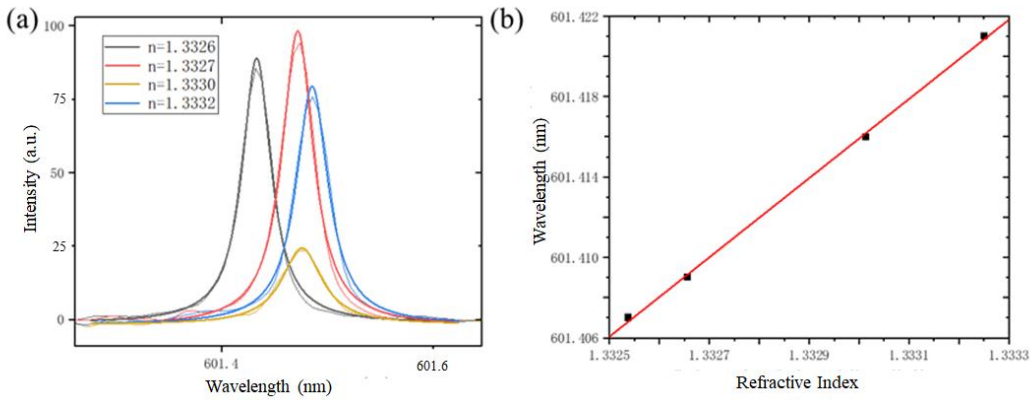

Figure 26 Wavelength shifts of circular-microcavity based microlaser sensor with respect to the change of external refractive index.

wavelengths of the peaks corresponding to the five solutions were 601.407 nm, 601.409 nm, 601.416 nm and 601.421 nm. Here we selected the wavelength of the highest peak from a group of spectral peaks as the sensing signal, since this main peak is relatively stable. On the other hand, it is difficult for our current WGM microlaser sensors to use a group of peaks for signal demodulation, as it has some spectral peaks of high-order WGMs.

The relationship between the position of the laser spectral peaks and the refractive index was then fitted with a linear fit. **Figure** 26 (b) shows that the five points have very good linearity and the linear fit has an R^2 of 0.99956. According to the fitted results, the refractive index sensitivity of our circular microcavity laser-based sensor is shown to be about 19.69 nm/RIU.

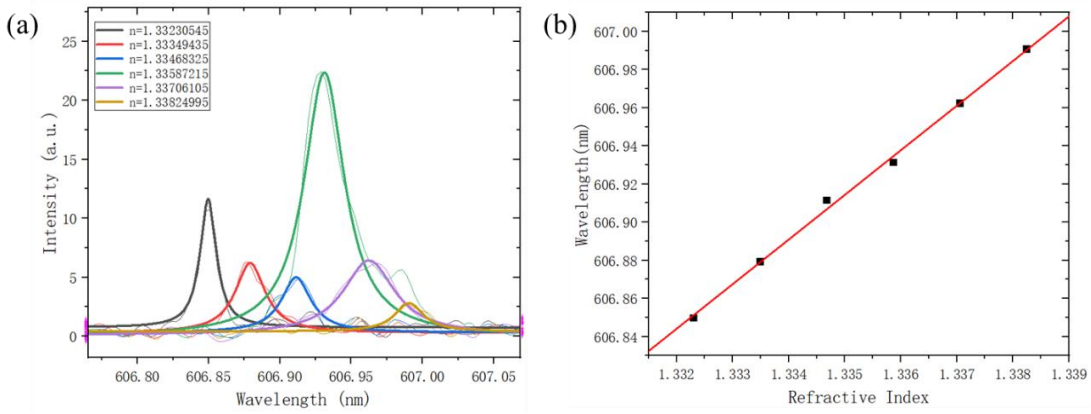

Figure 27 Wavelength shifts of Limacon-shaped microlaser sensor with respect to the change of external refractive index.

For Limacon-shaped microlaser, the experimentally measured data are shown in **Figure** 27 (a), and all the spectral lines are plotted onto the same graph. A regular shift of the laser peak near 606.8 nm – 607.0 nm occurred. As shown in the figure, after Lorentzian fitting, the center wavelengths of the peaks corresponding to the solutions were 606.85 nm, 606.88 nm, 606.91 nm, 606.93 nm, 606.96 nm and 606.99 nm.

The relationship between the position of the laser spectral peaks and the refractive index was then fitted with a linear fit. **Figure** 27 (b) shows that the six points have very good linearity, and the linear fit has an R^2 of 0.99744. According to the fitted results, the refractive index sensitivity of our Limacon-shaped microcavity laser-based sensor is shown to be about 23.40 nm/RIU. Our sensor has a slightly higher refractive index sensitivity compared to similar work [31]. The sensitivity could be further increased if the 3D micro-printing technology can be further improved to make smaller WGM microcavities.

5.3 Detection of Human Immunoglobulin G

Ultra-sensitive specificity detection of certain kinds of biomarkers may be important for early diagnosis of some disease [22].For example, Human IgG (150 kDa) are a class of globulins that have antibody activity or a chemical structure similar to that of antibodies, and are the main reactive substances in the humoral immune response.[77]. So, we used our deformed microlaser biosensor to specifically detect human IgG. In order to achieve specific detection of human IgG, we need to functionalize the surface of the microlaser with an antibody specific for human IgG. The specific detection is realized by the specific binding relationship between goat anti-human IgG and human IgG. Here, we used APTES solution at a concentration of 4% for surface activation. After that, 100μg/mL of goat anti-human IgG solution (dissolved in PBS) was used for surface functionalization. After the functionalization

process, we used different concentrations of human IgG solution for testing. When an antigen-antibody binding reaction occurs on the surface of the microlaser, the wavelength of the WGM will shift, and by observing this spectral shift in a spectrometer, specific detection of very low concentrations of biomarkers can be achieved.

In our experiments, the concentrations of the tested samples, the human IgA solutions, were set to 1 ag/mL, 10 ag/mL, 100 ag/mL, 1 fg/mL, 10 fg/mL, 100 fg/mL, 1 pg/mL, 10 pg/mL, 100 pg/mL, 1 ng/mL and 10 ng/mL in PBS, respectively.

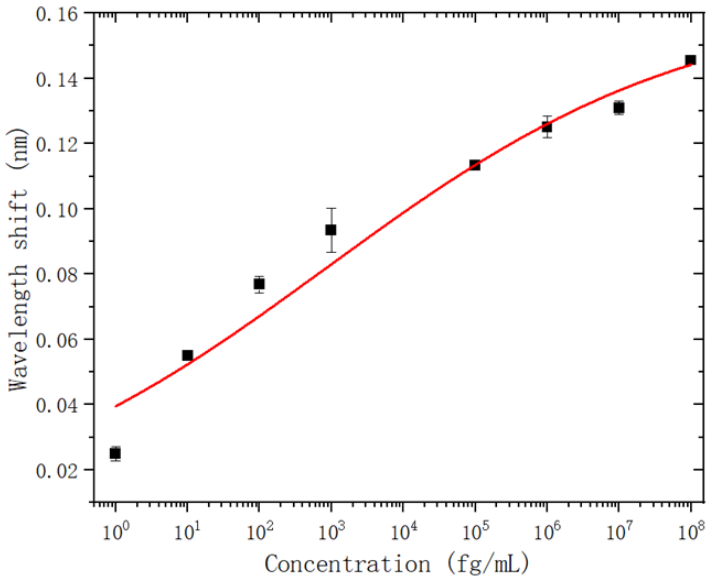

Figure 28. Wavelength shift of circular WGM microlaser sensor with respect to the change of the concentrations of human IgG in PBS. Data are fitted by red curve obtained from the Hill model ($R^2 = 0.9865$).

Figure 28 shows the experimental results of the sensing for human IgG done by a sensor based on our circular microlaser. This image shows the displacement of the peaks in the excitation spectral line with the concentration of human IgG solution. We fit the results using one of the most commonly used adsorption curves (Hill model), and the consistency of the obtained fits is quite ideal ($R^2 = 0.9865$). As can be seen from the images, after about 10 ng/mL, the peaks of the spectral lines stabilize as the solution concentration continues to increase,

which proves that the assay of our experiment is specific. The limit of detection of our sensor was measured as low as 1fg/mL (6.67 $\times 10^{-18}$M). In the figure, for each concentration we performed three independent experiments to obtain error bars. From Figure 28, the sensitivity of the linear variation region is S_{IgG-1} = 0.0022nm·mL·fg^{-1}. So that the theoretical DL can be estimated as $DL_{IgG-1} = 3\sigma/S_{IgG-1}$= 3.504fg/mL (23.36aM).

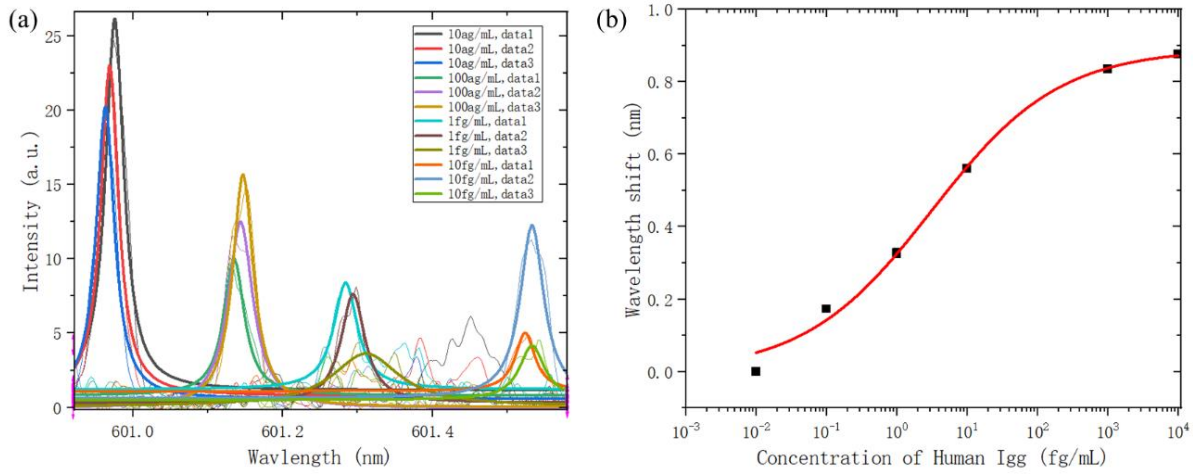

Figure 29 (a) Emission spectra of Limacon-shaped microlaser sensor with respect to the change of concentration of human Igg in PBS; (b) Wavelength shift of the microlaser sensor with respect to the change of the concentrations of human Igg in PBS. Data are fitted by red curve obtained from the Hill model ($R^2 = 0.9947$).

Using a similar experimental procedure, we tested the ability of a Limacon-shaped microlaser sensor to detect human IgG. **Figure** 29 shows the relationships between the wavelength shift and the concentrations of the human IgG. Similarly, we fit the results using one of the most commonly used adsorption curves (Hill model), and the consistency of the obtained fits is even more ideal (R^2= 0.9947). As can be seen from the images, after about 1 ng/mL, the peaks of the spectral lines stabilize as the solution concentration continues to increase, which proves that the assay of our experiment is specific. The limit of detection of our sensor was measured as low as 10 ag/mL (6.67 × 10^{-20}M). The results were obviously

better than that of circular microlaser based sensor. As mentioned before, for each concentration we performed three independent experiments to obtain error bars. The sensitivity of the linear variation region here is S_{IgG-2}= 0.0064 nm·mL·ag^{-1}. So that the theoretical DL is estimated to be $DL_{IgG-2}= 3\sigma/S_{IgG-2}$ = 15.94ag/mL (0.106aM). These results show that compared to circular microcavity lasers, sensors based on deformed microcavity lasers have a better performance in the field of very high sensitivity monitoring of biomarkers.

5.4 Summary

In this chapter, we have discussed the detection capabilities of cavity-deformed WGM microlaser sensors in label-free biodetection. First, we present the design of our WGM microlaser sensor that is standalone and allows for rapid on-chip integrated detection of proteins. In the experiments, we have demonstrated that this sensor has a very ideal stability in a PBS buffer environment, which is the foundation of this sensor's ability for highly sensitive biodetection. Sensitivity tests have shown that such cavity-deformed WGM microlaser sensors have a very high sensitivity to the change of the refractive index of external environment. The results demonstrated above indicate the excellent performance of cavity-deformed WGM microlaser sensors for high-sensitivity biosensing. Finally, specific detection experiments with Human Igg demonstrated that our sensor can detect biomarkers on the order of 0.1 aM.

Chapter 6. Conclusion and future outlooks

In this thesis, two kinds of deformed optical microcavities, i.e., Limacon-shaped microcavity and elliptical microcavity, have been studied to develop WGM microlaser sensors for label-free biomarker sensing applications. Thanks to our own-built DMD-based digital optical 3D micro-printing system, which has the advantages including flexibility in photomask free, rapid fabrication of 3D microstructures, and relatively low cost, we developed a new technology in fabrication of standalone SU-8 WGM microcavity sensors. We have systematically investigated the dependency of the directional emission on the geometry of WGM cavity numerically, which can be used to improve the efficiency of the coupling between the microcaivity and optical fiber. Through numerical simulations performed using COMSOL Multiphysics, we have designed weakly deformed WGM microcavities that can achieve both directional emission and high Q value. Then, the designed WGM microcavities have been fabricated by using our own-built optical 3D micro-printing technology.

It was experimentally demonstrated that, both kinds of weakly deformed microcavities fabricated by our 3D micro-printing system can be used to make low-threshold WGM microlasers in visible wavelength by further depositing with a laser-dye doped SU8. By proper optimization of their geometries, higher Q microlaser sensors with directional emission ability have been achieved. The highest Q factor can reach around 10^5. The label-free biodetection ability of such WGM microlaser sensors have also been tested in experiments. In addition to the characterization of the sensor's bulk sensitivity, the WGM microlaser sensors have also been modified to selectively detect biomarkers. Experiments showed that such WGM microlaser biosensor can achieve an impressive detection limit of 15.94 ag/mL in the detection of human IgG.

These results showed great promises of the WGM microlaser sensors. In future works, to further improve the performance of such WGM microlaser sensors, the first important thing is to continue the improvement of the performance of WGM microlaser sensors. For example, better geometry and size of WGM microcavity can be pursued to maintain directional emission while having a higher Q value. Alternatively, the use of a different material, such as SiO_2 with lower material loss, can be considered to improve the Q value of the microcavity. In addition to this, better photoluminescent materials with higher quantum efficiency, such as perovskite and aggregation-induced-emission materials, can also be considered as the gain medium to improve the better lasing efficiency of the laser to let the sensor working at lower pumping power.

In addition to this, another important direction for such WGM microlaser sensors is to integrate such WGM microlaser sensor with microfluidic chips to develop optofluidic biochips. Microfluidic chips have the advantages of savings in assay samples, flexibility in sample pretreatment and delivery. Technologies combining high-Q WGM optical microlaser sensors and microfluidic chips are expected to provide solutions for portable, ultra-sensitive biomarker detection, which may find great many applications in the fields of early diagnosis of disease and health monitoring, etc.

References

[1] W. Fritzsche *et al.*, "Chip systems for analysis of nucleic acids with integrated amplification and detection," *Springer Science & Business Media,* pp. 289-304, 2012.

[2] J. Godin, C. H. Chen, S. Cho, W. Qiao, F. Tsai, and Y. Lo, "Microfluidics and photonics for Bio-System-on-a-Chip: A review of advancements in technology towards a microfluidic flow cytometry chip," *Journal of biophotonics,* vol. 1, no. 5, pp. 355-376, 2008.

[3] S. Nizamoglu *et al.*, "Bioabsorbable polymer optical waveguides for deep-tissue photomedicine," *Nature communications,* vol. 7, no. 1, p. 10374, 2016.

[4] J. Wu, M. Yao, F. Xiong, A. Zhang, H. Tam, and P. Wai, "Optical fiber-tip Fabry–Perot interferometric pressure sensor based on an in situ μ-printed air cavity," *Journal of Lightwave Technology,* vol. 36, no. 17, pp. 3618-3623, 2018.

[5] K. Vahala, "Optical microcavities," *nature,* vol. 424, no. 6950, pp. 839-846, 2003.

[6] E. Lafalce *et al.*, "Robust lasing modes in coupled colloidal quantum dot microdisk pairs using a non-Hermitian exceptional point," *nature communications,* vol. 10, no. 1, p. 561, 2019.

[7] D. Cole, E. Lamb, P. Del'Haye, S. Diddams, and S. Papp, "Soliton crystals in Kerr resonators," *Nature Photonics,* vol. 11, no. 10, pp. 671-676, 2017.

[8] Y. Tung *et al.*, "Optofluidic detection for cellular phenotyping," *Lab on a Chip,* vol. 12, no. 19, pp. 3552-3565, 2012.

[9] C. Lv *et al.*, "Integrated optofluidic-microfluidic twin channels: toward diverse application of lab-on-a-chip systems," *Scientific Reports,* vol. 6, no. 1, p. 19801, 2016.

[10] X. Jiang, A. Qavi, S. Huang, and L. Yang, "Whispering-gallery sensors," *Matter,* vol. 3, no. 2, pp. 371-392, 2020.

[11] H. Hwang and J. Park, "Optoelectrofluidic platforms for chemistry and biology," *Lab on a Chip,* vol. 11, no. 1, pp. 33-47, 2011.

[12] Ş. Özdemir *et al.*, "Highly sensitive detection of nanoparticles with a self-referenced and self-heterodyned whispering-gallery Raman microlaser," *Proceedings of the National Academy of Sciences,* vol. 111, no. 37, pp. E3836-E3844, 2014.

[13] A. Armani, R. Kulkarni, S. Fraser, R. Flagan, and K. Vahala, "Label-free, single-molecule detection with optical microcavities," *science,* vol. 317, no. 5839, pp. 783-787, 2007.

[14] L. He, Ş. Özdemir, J. Zhu, W. Kim, and L. Yang, "Detecting single viruses and nanoparticles using whispering gallery microlasers," *Nature nanotechnology,* vol. 6, no. 7, pp. 428-432, 2011.

[15] Y. Xiao and Q. Gong, "Optical microcavity: from fundamental physics to functional photonics devices," *Science Bulletin,* vol. 61, pp. 185-186, 2016.

[16] S. Murphy and A. Atala, "3D bioprinting of tissues and organs," *Nature biotechnology,* vol. 32, no. 8, pp. 773-785, 2014.

[17] M. Marelli, N. Gadhari, G. Boero, M. Chiquet, and J. Brugger, "Cell force measurements in 3D microfabricated environments based on compliant cantilevers," *Lab on a Chip,* vol. 14, no. 2, pp. 286-293, 2014.

[18] J. Hohmann, M. Renner, E. Waller, and G. Freymann, "Three-Dimensional μ-Printing: An Enabling Technology," *Advanced Optical Materials,* vol. 3, no. 11, pp. 1488-1507, 2015.

[19] R. Palankar *et al.*, "3D Micropillars Guide the Mechanobiology of Human Induced Pluripotent Stem Cell-Derived Cardiomyocytes," *Advanced Healthcare Materials,* vol. 5, no. 3, pp. 335-341, 2016.

[20] N. Zhang *et al.*, "Far-field single nanoparticle detection and sizing," *Optica,* vol. 4, no. 9, pp. 1151-1156, 2017.
[21] A. Zhang *et al.*, "Rapid fabrication of complex 3D extracellular microenvironments by dynamic optical projection stereolithography," *Advanced materials,* vol. 24, no. 31, pp. 4266-4270, 2012.
[22] E. Melnik, R. Bruck, P. Müellner, T. Schlederer, R. Hainberger, and M. Lämmerhofer, "Human IgG detection in serum on polymer based Mach - Zehnder interferometric biosensors," *Journal of biophotonics,* vol. 9, no. 3, pp. 218-223, 2016.
[23] K. De Vos, I. Bartolozzi, E. Schacht, P. Bienstman, and R. Baets, "Silicon-on-Insulator microring resonator for sensitive and label-free biosensing," *Optics express,* vol. 15, no. 12, pp. 7610-7615, 2007.
[24] M. Foreman, J. Swaim, and F. Vollmer, "Whispering gallery mode sensors," *Advances in optics and photonics,* vol. 7, no. 2, pp. 168-240, 2015.
[25] S. Arnold, M. Khoshsima, I. Teraoka, S. Holler, and F. Vollmer, "Shift of whispering-gallery modes in microspheres by protein adsorption," *Optics letters,* vol. 28, no. 4, pp. 272-274, 2003.
[26] X. Ouyang *et al.*, "Ultrasensitive optofluidic enzyme-linked immunosorbent assay by on-chip integrated polymer whispering-gallery-mode microlaser sensors," *Lab on a Chip,* vol. 20, no. 14, pp. 2438-2446, 2020.
[27] V. Dantham, S. Holler, V. Kolchenko, Z. Wan, and S. Arnold, "Taking whispering gallery-mode single virus detection and sizing to the limit," *Applied Physics Letters,* vol. 101, no. 4, 2012.
[28] E. Kim, M. Baaske, I. Schuldes, P. Wilsch, and F. Vollmer, "Label-free optical detection of single enzyme-reactant reactions and associated conformational changes," *Science advances,* vol. 3, no. 3, p. e1603044, 2017.
[29] Y. Chen, U. Schoeler, C. Huang, and F. Vollmer, "Combining Whispering-Gallery Mode Optical Biosensors with Microfluidics for Real-Time Detection of Protein Secretion from Living Cells in Complex Media," *Small,* vol. 14, no. 22, p. 1703705, 2018.
[30] H. Ghali, H. Chibli, J. L. Nadeau, P. Bianucci, and Y. Peter, "Real-time detection of Staphylococcus aureus using Whispering Gallery Mode optical microdisks," *Biosensors*, vol. 6, no. 2, p. 20, 2016.
[31] Z. Guo *et al.*, "Hyperboloid-Drum Microdisk Laser Biosensors for Ultrasensitive Detection of Human IgG," *Small,* vol. 16, no. 26, p. 2000239, 2020.
[32] Y. Kim and H. Lee, "On-chip label-free biosensing based on active whispering gallery mode resonators pumped by a light-emitting diode," *Optics express,* vol. 27, no. 23, pp. 34405-34415, 2019.
[33] M. De Goede *et al.*, "Al 2 O 3: Yb 3+ integrated microdisk laser label-free biosensor," *Optics letters,* vol. 44, no. 24, pp. 5937-5940, 2019.
[34] E. Ozgur *et al.*, "Ultrasensitive detection of human chorionic gonadotropin using frequency locked microtoroid optical resonators," *Analytical chemistry,* vol. 91, no. 18, pp. 11872-11878, 2019.
[35] E. Ozgur, P. Toren, O. Aktas, E. Huseyinoglu, and M. Bayindir, "Label-free biosensing with high selectivity in complex media using microtoroidal optical resonators," *Scientific reports,* vol. 5, no. 1, p. 13173, 2015.
[36] S. Suebka, P.-D. Nguyen, A. Gin, and J. Su, "How fast it can stick: Visualizing flow delivery to microtoroid biosensors," *ACS sensors,* vol. 6, no. 7, pp. 2700-2708, 2021.

[37] Y. Wang, H. Zhang, Y. Cui, W. Lin, B. Liu, and D. Xiang, "Real-time conformational change monitoring of G-quadruplex using capillary-based biocompatible whispering gallery mode microresonator," *IEEE Sensors Journal,* vol. 20, no. 21, pp. 12558-12564, 2020.

[38] J. Suter *et al.*, "Label-free quantitative DNA detection using the liquid core optical ring resonator," *Biosensors and Bioelectronics,* vol. 23, no. 7, pp. 1003-1009, 2008.

[39] H. Zhu, I. White, J. Suter, P. Dale, and X. Fan, "Analysis of biomolecule detection with optofluidic ring resonator sensors," *Optics Express,* vol. 15, no. 15, pp. 9139-9146, 2007.

[40] L. Fu, Q. Lu, X. Liu, X. Chen, X. Wu, and S. Xie, "Combining whispering gallery mode optofluidic microbubble resonator sensor with GR-5 DNAzyme for ultra-sensitive lead ion detection," *Talanta,* vol. 213, p. 120815, 2020.

[41] H. Wan *et al.*, "Label-free, ultra-low detection limit DNA biosensor using high quality optical microcavity functionalized by DNA tetrahedral nanostructure probes," *Nanophotonics,* no. 0, 2023.

[42] S. Geidel *et al.*, "Integration of an optical ring resonator biosensor into a self-contained microfluidic cartridge with active, single-shot micropumps," *Micromachines,* vol. 7, no. 9, p. 153, 2016.

[43] S. Wu, Y. Guo, W. Wang, J. Zhou, and Q. Zhang, "Label-free biosensing using a microring resonator integrated with poly-(dimethylsiloxane) microfluidic channels," *Review of Scientific Instruments,* vol. 90, no. 3, 2019.

[44] H. Zhu, I. White, J. Suter, M. Zourob, and X. Fan, "Opto-fluidic micro-ring resonator for sensitive label-free viral detection," *Analyst,* vol. 133, no. 3, pp. 356-360, 2008.

[45] J. Gohring, P. Dale, X. Fan, and A. Chemical, "Detection of HER2 breast cancer biomarker using the opto-fluidic ring resonator biosensor," *Sensors and Actuators B: Chemical,* vol. 146, no. 1, pp. 226-230, 2010.

[46] H. Li and X. Fan, "Characterization of sensing capability of optofluidic ring resonator biosensors," *Applied Physics Letters,* vol. 97, no. 1, 2010.

[47] A. Ksendzov and Y. Lin, "Integrated optics ring-resonator sensors for protein detection," *Optics letters,* vol. 30, no. 24, pp. 3344-3346, 2005.

[48] Y. Zhi, X.-C. Yu, Q. Gong, L. Yang, and Y. Xiao, "Single Nanoparticle Detection Using Optical Microcavities," *Advanced Materials,* vol. 29, no. 12, p. 1604920, 2017/03/01 2017.

[49] F. Vollmer, D. Braun, A. Libchaber, M. Khoshsima, I. Teraoka, and S. Arnold, "Protein detection by optical shift of a resonant microcavity," *Applied Physics Letters,* Article vol. 80, no. 21, pp. 4057-4059, May 27 2002.

[50] J. Gohring, P. S. Dale, and X. Fan, "Detection of HER2 breast cancer biomarker using the opto-fluidic ring resonator biosensor," *Sensors and Actuators B: Chemical,* vol. 146, no. 1, pp. 226-230, 2010/04/08/ 2010.

[51] V. R. Dantham, S. Holler, C. Barbre, D. Keng, V. Kolchenko, and S. Arnold, "Label-Free Detection of Single Protein Using a Nanoplasmonic-Photonic Hybrid Microcavity," *Nano Letters,* vol. 13, no. 7, pp. 3347-3351, Jul 2013.

[52] A. L. Washburn, M. S. Luchansky, A. L. Bowman, and R. Bailey, "Quantitative, Label-Free Detection of Five Protein Biomarkers Using Multiplexed Arrays of Silicon Photonic Microring Resonators," *Analytical Chemistry,* Article vol. 82, no. 1, pp. 69-72, Jan 1 2010.

[53] E. Nuhiji and P. Mulvaney, "Detection of unlabeled oligonucleotide targets using whispering gallery modes in single, fluorescent microspheres," *Small,* Article vol. 3, no. 8, pp. 1408-1414, Aug 2007.

[54] M. Murib *et al.*, "Photonic detection and characterization of DNA using sapphire microspheres," *Journal of Biomedical Optics,* Article vol. 19, no. 9, Sep 2014, Art. no. 097006.
[55] M. Schubert *et al.*, "Monitoring contractility in cardiac tissue with cellular resolution using biointegrated microlasers," *Nature Photonics,* vol. 14, no. 7, pp. 452-458, 2020.
[56] Y. Wu, D. Zhang, P. Yin, and F. Vollmer, "Ultraspecific and Highly Sensitive Nucleic Acid Detection by Integrating a DNA Catalytic Network with a Label-Free Microcavity," *Small,* Article vol. 10, no. 10, pp. 2067-2076, May 28 2014.
[57] J. Zhang *et al.*, "Whispering-gallery nanocavity plasmon-enhanced Raman spectroscopy," *Scientific Reports,* Article vol. 5, Oct 7 2015, Art. no. 15012.
[58] M. D. Baaske, M. Foreman, and F. Vollmer, "Single-molecule nucleic acid interactions monitored on a label-free microcavity biosensor platform," *Nature Nanotechnology,* Article vol. 9, no. 11, pp. 933-939, Nov 2014.
[59] F. Vollmer, S. Arnold, and D. Keng, "Single virus detection from the reactive shift of a whispering-gallery mode," *Proceedings of the National Academy of Sciences*, vol. 105, no. 52, pp. 20701-20704, 2008.
[60] T. Lu *et al.*, "High sensitivity nanoparticle detection using optical microcavities," *Proceedings of the National Academy of Sciences of the United States of America,* Article vol. 108, no. 15, pp. 5976-5979, Apr 12 2011.
[61] V. Dantham, S. Holler, V. Kolchenko, Z. Wan, and S. Arnold, "Taking whispering gallery-mode single virus detection and sizing to the limit," *Applied Physics Letters,* Article vol. 101, no. 4, Jul 23 2012, Art. no. 043704.
[62] J. Mandana and E. Daniel, "Early stage, label-free detection of breast cancer based on exosome's protein content alteration," in *Proc.SPIE*, 2022, vol. 12139, p. 121390G.
[63] Z. Wang *et al.*, "Autonomous Microlasers for Profiling Extracellular Vesicles from Cancer Spheroids," *Nano Letters,* vol. 23, no. 7, pp. 2502-2510, 2023/04/12 2023.
[64] E. Smith, S. Schulze, S. Kiravittaya, Y. Mei, S. Sanchez, and O. Schmidt, "Lab-in-a-Tube: Detection of Individual Mouse Cells for Analysis in Flexible Split-Wall Microtube Resonator Sensors," *Nano Letters,* Article vol. 11, no. 10, pp. 4037-4042, Oct 2011.
[65] S. Lee *et al.*, "Universal output directionality of single modes in a deformed microcavity," *Physical Review A,* vol. 75, no. 1, p. 011802, 2007.
[66] X. Jiang, C. Zou, L. Wang, Q. Gong, and Y. Xiao, "Whispering-gallery microcavities with unidirectional laser emission," *Laser Photonics Reviews,* vol. 10, no. 1, pp. 40-61, 2016.
[67] X. Jiang *et al.*, "Highly unidirectional emission and ultralow-threshold lasing from on-chip ultrahigh-Q microcavities," *Advanced Materials,* vol. 24, no. 35, p. OP260, 2012.
[68] J. Liu *et al.*, "Process research of high aspect ratio microstructure using SU-8 resist," *Microsystem Technologies,* vol. 10, no. 4, pp. 265-268, 2004/05/01 2004.
[69] J. Lee, K. Choi, and K. Yoo, "Innovative SU-8 Lithography Techniques and Their Applications," *Micromachines,* vol. 6, no. 1, pp. 1-18, 2014.
[70] J. Greener *et al.*, "Rapid, cost-efficient fabrication of microfluidic reactors in thermoplastic polymers by combining photolithography and hot embossing," *Lab Chip,* vol. 10, no. 4, pp. 522-524, 2010.
[71] A. Campo and C. Greiner, "SU-8: a photoresist for high-aspect-ratio and 3D submicron lithography," *Journal of Micromechanics and Microengineering,* vol. 17, no. 6, pp. R81-R95, 2007.

[72] M. Nordström *et al.*, "SU-8 Cantilevers for Bio/chemical Sensing; Fabrication, Characterisation and Development of Novel Read-out Methods," *Sensors,* vol. 8, no. 3, pp. 1595-1612, 2008.

[73] S. Chung and S. Park, "Effects of temperature on mechanical properties of SU-8 photoresist material," *Journal of Mechanical Science and Technology,* vol. 27, no. 9, pp. 2701-2707, 2013/09/01 2013.

[74] S. Keller, G. Blagoi, M. Lillemose, D. Haefliger, and A. Boisen, "Processing of thin SU-8 films," *Journal of Micromechanics and Microengineering,* vol. 18, no. 12, p. 125020, 2008/11/14 2008.

[75] N. Sakai, T. Sakai, Y. Osamura, and S. Yamamoto, "Detection of C6H–toward the Low-Mass Protostar IRAS 04368+ 2557 in L1527," *The Astrophysical Journal,* vol. 667, no. 1, p. L65, 2007.

[76] Y. Yeh, "Real-time measurement of glucose concentration and average refractive index using a laser interferometer," *Optics Lasers in Engineering,* vol. 46, no. 9, pp. 666-670, 2008.

[77] H. M. Wong, J. Wang, and C. Wang, "In vitro sustained release of human immunoglobulin G from biodegradable microspheres," *Industrial engineering chemistry research,* vol. 40, no. 3, pp. 933-948, 2001.